

The organisation of subglacial drainage during the demise of the Finnish Lake District Ice-Lobe

Adam J. Hepburn^{1,2*}, Christine F. Dow¹, Antti Ojala³, Joni Mäkinen³, Elina Ahokangas³, Jussi Hovikoski⁴, Jukka-Pekka Palmu⁴, and Kari Kajuuutti³

¹Department of Geography and Environmental Management, University of Waterloo, Waterloo, ON, Canada

²European Space Astronomy Centre, European Space Agency, Madrid, Spain

³Department of Geography and Geology, University of Turku, Turku, Finland

⁴Geological Survey of Finland, Espoo, Finland

Correspondence: Adam J. Hepburn, now at Aberystwyth University, Aberystwyth, Wales, UK (adam.hepburn@aber.ac.uk)

Abstract. Unknown basal characteristics limit our ability to simulate the subglacial hydrology of rapidly melting contemporary ice sheets. Sediment-based landforms generated beneath Late Pleistocene ice sheets, together with detailed digital elevation models, offer a valuable means of testing basal hydrology models, which describe the flow and dynamics of water in the subglacial system. However, to date no work has evaluated how well process-based subglacial hydrology models represent

5 the hypothesised conditions associated with glaciofluvial landform formation in the palaeo setting. Previous work comparing model output to geomorphological evidence has typically done so using models which do not resolve subglacial processes and instead express likely subglacial water pathways. Here, we explore the ability of the Glacier Drainage System model (GlaDS), a process based subglacial hydrology model, to represent the genesis conditions associated with a specific glaciofluvial landform termed ‘murtoos’. Distinctive triangular landforms found throughout Finland and Sweden, murtoos are hypothesised to form
10 40–60 km from the former Fennoscandian Ice Sheet margin within a ‘semi-distributed’ system at the onset of channelised drainage, in small cavities where water pressure is equal to or exceeds ice overburden pressure. Concentrating within a specific ice lobe of the former Fennoscandian Ice Sheet and using digital elevation models with a simulated former ice surface geometry, we forced GlaDS with transient surface melt and explored the sensitivity of our model outcomes to parameter decisions such as the system conductivity and bed topography. Our model outputs ~~represents many of closely match the general spacing, direction and complexity of eskers and mapped assemblages of features related to subglacial drainage in ‘meltwater routes’~~. Many of
15 the predictions for murtoos ~~origin~~ information are produced by the model, including the location of water pressure equal to ice overburden, the onset of channelised drainage, ~~and~~ the transition in drainage modes. ~~Modelled channels also closely match the general spacing, direction and complexity of eskers and mapped assemblages of features related to subglacial drainage in ‘meltwater routes’~~. Further, these ~~and importantly, the seasonal sequence of drainage conditions inferred from murtoos~~
20 ~~sedimentology~~. These conclusions are largely robust to a range of parameter decisions ~~and we explore seasonal and inter-annual drainage behaviour associated with murtoos zones and meltwater pathways~~. Our results demonstrate that examining palaeo basal topography alongside subglacial hydrology model outputs holds promise for the mutually beneficial analyses of palaeo and contemporary ice sheets to assess the controls of hydrology on ice dynamics and subglacial landform evolution.

1 Introduction

25 The changing configuration of the basal hydrological system beneath ice sheets throughout the melt season is primarily responsible for modulating the response of ice flow to meltwater input (Schoof, 2010). Subglacial water is typically conceptualised as being routed through either *distributed*, inefficient, and high water pressure systems (Weertman, 1972; Kamb, 1987; Boulton and Jones, 1979), or *channelised*, efficient, and lower water pressure systems (Nye, 1972; Röthlisberger, 1972; Hooke, 1989), transitioning between the two as a function of discharge (Schoof, 2010). The seasonal delivery of meltwater to the bed of ice sheets, and transition of subglacial hydrological systems in response, exerts a first order control on ice flow by modifying the frictional resistance to ice flow (Schoof, 2010). Understanding where and when transitions between distributed and channelised drainage occur beneath ice sheets is critical if such processes are going to be faithfully represented in ice sheet models used to predict the rate and timing of ice sheet mass loss (Andrews et al., 2014; Nienow et al., 2017), particularly in response to more widespread and prolonged atmospheric warming (e.g., van den Broeke et al., 2023).

35 To date, most analyses of seasonal subglacial hydrological development ~~has have~~ been applied to contemporary ice sheets and glaciers. However, these sites lack key information about basal characteristics, such as basal topography, underlying sedimentology, and the hydraulic properties of the subsurface material (Chu, 2014). Subglacial hydrology models are often used to analyse these systems at the catchment scale but, given the absence of more detailed information, basal characteristics are often reduced to parameterisations, or simplifications, of what is likely a more complex reality (e.g., Schoof, 2010; Werder et al., 2013; Flowers, 2018; Kazmierczak et al., 2022).

40 Glaciated Late Pleistocene terrains may provide a valuable insight into the subglacial hydrological processes operating beneath ice sheets (Stokes et al., 2015; Greenwood et al., 2016), ~~potentially including those variable at the sub-annual scale and across the distributed–channelised transition~~. Numerical ice sheet models are already evaluated against the rich geomorphological record that Late Pleistocene ice sheets left behind, particularly landforms relating to ice flow direction or ice marginal position (e.g., Boulton and Haggdorn, 2006; Kleman et al., 2006; Tarasov et al., 2012; Gandy et al., 2019, 2021; Archer et al., 2023; García-Ruiz et al., 2023). Glaciofluvial landforms are especially common in the landform record (e.g., Clark and Walder, 1994; Cofaigh, 1996; Rampton, 2000; Utting et al., 2009; Coughlan et al., 2020; Dewald et al., 2021, 2022) and may represent ideal targets against which to evaluate subglacial hydrology models, potentially including processes variable at sub-annual scales and across the distributed–channelised transition (Kleman et al., 2006; Bingham et al., 2010; Stokes et al., 2015). However, landform genesis ~~is typically uncertain (e.g., Cofaigh, 1996) and comparing geomorphology to subglacial hydrology model output is further complicated by the time-integrated and heavily channelised nature of the glaciofluvial record (Stokes et al., 2015; Greenwood et al., 2016)~~ uncertainty arises from both fundamentally different concepts of how a landform is formed and the variable spatial and temporal scales of formation (Cofaigh, 1996; Stokes et al., 2015; Greenwood et al., 2016)

55 Previous work has largely used relatively simple models to subglacial hydrology to explore the spatial expression of channelised glaciofluvial landforms. These models often make assumptions about the configuration of the drainage system (Stokes et al., 2015) and do not explicitly resolve channel formation or exchanges between drainage systems. Typically, such models

operate by prescribing a fixed water pressure at or near overburden everywhere, resulting in an expression of likely flow routing but not physical channel development or evolution (e.g., Livingstone et al., 2013a, b, 2015; Karlsson and Dahl-Jensen, 2015; 60 Shackleton et al., 2018; Kirkham et al., 2022). Alternatively, in models where water pressure is allowed to vary, channels are assumed to form where water pressure is equal to ice overburden pressure but the process of channel formation is not explicitly resolved (e.g., Boulton et al., 2007a, b, 2009). These models are unable to capture dynamic drainage changes, and are instead intended to represent long-term, interannual, ‘steady-state’ conditions (Banwell et al., 2013). More complex models have been used to address esker formation over shorter timescales in 1D (e.g., Beaud et al., 2018; Hewitt and Creyts, 2019) while 2D 65 models which include exchanges between a distributed system and a single channel have been used to interrogate esker length ~~and~~ spacing scaling relationships (e.g., Hewitt, 2011) and erosion rates associated with subglacial drainage efficiency (e.g., Beaud et al., 2014). However, these more complex models use idealised parabolic ice surfaces, often with a flat bed. ~~Despite the widespread application of~~ In contrast, modern subglacial hydrology models (*i.e.*, those capable of resolving transitions between distributed and channelised drainage in both space and time) are widely applied to contemporary ice sheets (e.g., 70 Flowers, 2018; Indrido et al., 2021; Dow et al., 2022; Sommers et al., 2022; Ehrenfeucht et al., 2023), ~~and~~. However, despite the critical need to evaluate and improve these modern subglacial hydrology models using all available sources of data (Dow, 2023), we are not aware of previous work which has evaluated the ability of ~~modern subglacial hydrology~~ such models to reproduce the subglacial conditions (e.g., water pressure, channel location) associated with glaciofluvial landform formation.

In this paper we apply the Glacier Drainage System model (GlaDS Werder et al., 2013)—a modern subglacial hydrology 75 model capable of resolving the transition between channelised and distributed drainage—to a palaeo ice sheet terrain. We evaluate the ability of GlaDS to represent the conditions giving rise to specific glaciofluvial landforms by making comparisons between model output and the spatial expression and predicted generation of ‘murtoos’ (singular: murtoo, Mäkinen et al., 2017; Ojala et al., 2019) recently identified in Fennoscandia. More widely described channelised features such as eskers (e.g., Storrar and Livingstone, 2017) and tunnel valleys (e.g., Kirkham et al., 2022, 2024) often exceed 10 km in length and likely 80 represent ~~continuous~~ time-transgressive formation over decades–millennia of ice-sheet margin retreat (Mäkinen, 2003). In contrast, murtoos are small (<100 m) ~~glaciofluvial~~ glaciofluvial landforms thought to represent the spatiotemporal transition from distributed to channelised subglacial drainage over as little as one melt season (Hovikoski et al., 2023; Mäkinen et al., 2023). The size, formation rate, spatial distribution, and sedimentological architecture of murtoos provide a unique set of predictions against which a subglacial hydrology model can be tested (Hovikoski et al., 2023), including the location of a 85 persistent area of high water pressure, the evolution of discharge through the year, and the spatial onset of channelised drainage. The aim of this paper is to explore the ability of GlaDS, a process based subglacial hydrology model, to explain murtoo formation in both space and time.

2 The glaciofluvial significance of murtoos

Clearly distinguishable from other glaciofluvial landforms, murtoos are small (30–100 m in width/length), low relief (~5 m 90 high) features orientated parallel to ice flow with a distinctive, broadly triangular morphology (See Figure 1, & Ojala et al.,

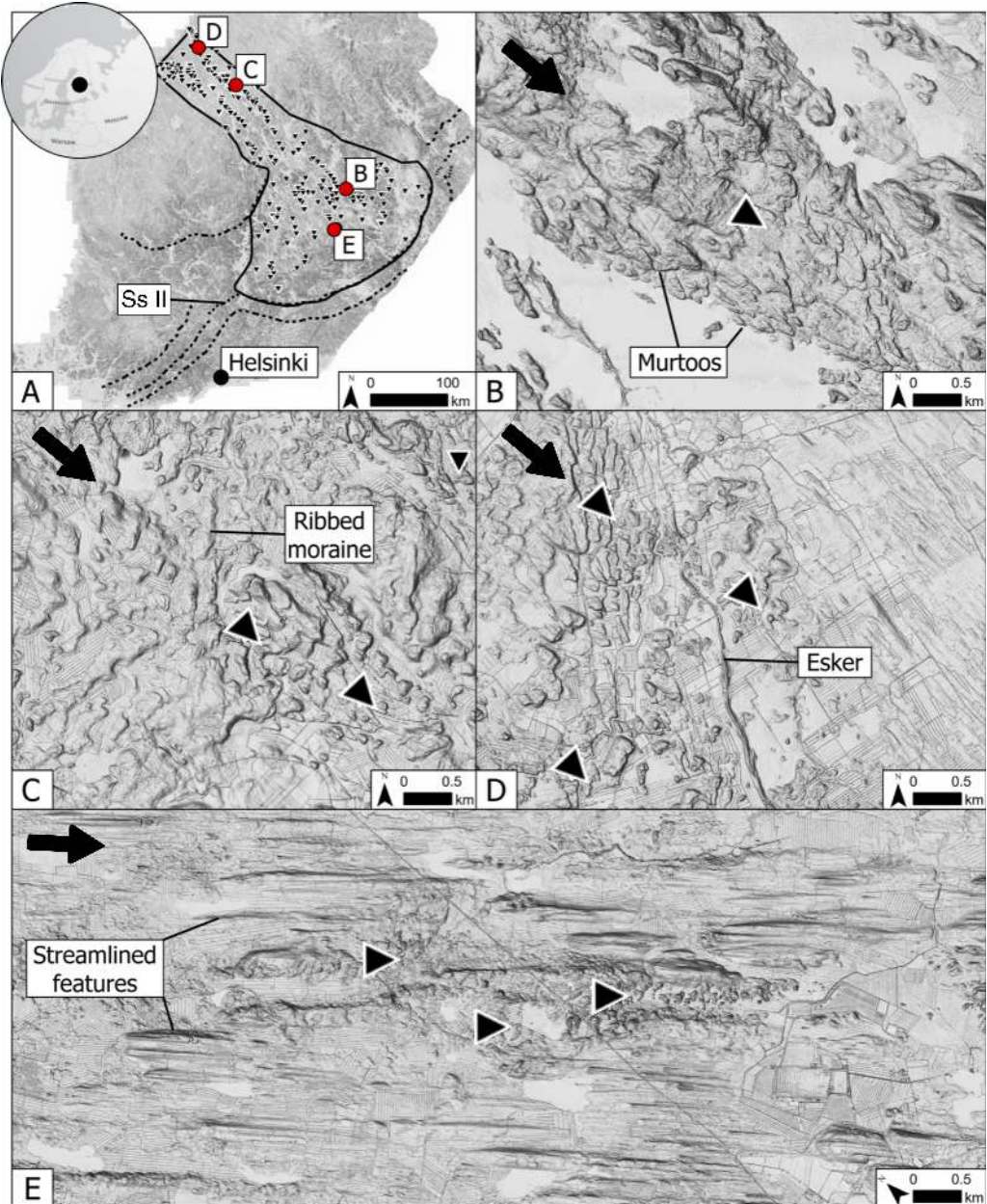


Figure 1. The study area. **A)** The extent of the GlaDS model domain (solid line) in the Finnish Lake District Ice Lobe (FLDIL) and the Salpausselkä (dashed line). Salpausselkä II (Ss II) marks the 12 cal. ka ice extent. Murtoos fields identified by Ahokangas et al. (2021) within the FLDIL are shown as inverted triangles. **B)** A murtoos field. Adjacent to the murtoos, a large esker is visible in the lake. **C)** Murtoos fields amongst ribbed moraines in the north of the FLDIL. **D)** An abrupt downstream transition from murtoos fields to a large esker. Additional murtoos fields are found directly adjacent to the esker. **E)** Three murtoos fields amongst streamlined terrain within at the centre of the FLDIL. All panels show a multi-directional oblique weighted hillshade based on 2 m LiDAR data (see Ahokangas et al., 2021, for details). In panels B–E, black arrows in the upper left corner of each panel indicate the approximate ice flow direction and the inverted triangles are aligned with the orientation of murtoos fields.

2019, 2021, 2022; Ahokangas et al., 2021; Peterson Becher and Johnson, 2021; Vérité et al., 2022; Van Boeckel et al., 2022). Mapping across Finland and Sweden (Mäkinen et al., 2017; Peterson et al., 2017; Ahokangas et al., 2021) reveals a preferential clustering of murtoos in swarms or fields (e.g., Figure 1B) along subglacial meltwater routes—integrated assemblages of multiple landforms associated with subglacial meltwater (Lewington et al., 2020; Ahokangas et al., 2021; Dewald et al., 2022).
95 Subglacial meltwater routes containing murtoos, or ‘*murtoo routes*’ (Ahokangas et al., 2021) are concentrated in faster flowing, warm-based sectors of the Fennoscandian ice sheet (FIS) and are often adjacent to, or downstream of, drumlin fields or ribbed moraines (e.g., Vérité et al., 2022, and Figure 1C). Murtoo routes are also often located upstream of, and appear to transition into, eskers (e.g., Ahokangas et al., 2021, and Figure 1D). Crucially, murtoo routes are rarely found closer than 40–60 km ~~of to~~ the former FIS ice margins (Mäkinen et al., 2023), aligning well with the maximum observed length of channels (~50 km)
100 in contemporary Greenland (e.g., Chandler et al., 2013, 2021; Dow et al., 2015).

The sedimentological sequence of a murtoo (as described in Hovikoski et al., 2023, and summarised in Table 1) is characterised by abrupt changes in sedimentary structure and grain size and charts the spatiotemporal transition from distributed to increasingly channelised flow within a single melt season during deglaciation (Mäkinen et al., 2023). Murtoos typically comprise a core unit containing sorted sediments, which develops at the end of meltwater pulses within a rapidly enlarging broad subglacial conduit. This core represents the first ~~stage-phase~~ of murtoo formation and evidences at least partial ice contact and periodic deformation (Hovikoski et al., 2023). Following the onset of spring melt, pulses of water deposit a main body unit (~~referred to as Unit 2 by Mäkinen et al., 2023~~) (murtoo developmental phase 2 in Table 1 and referred to as Unit 2 by Mäkinen et al., 2023) that i) distally is comprised of alternating facies of heterogeneous diamicton, with strong fabrics interbedded with sorted gravelly and sandy sediment and ii) proximally is comprised of alternating sequences of glaciofluvial deposits, with current ripples (formed in low discharge, lower flow regimes) giving way to transitional cross-bedding (transitional flow regimes), and antitidunal sinusoidal lamination (formed in higher discharge, upper flow regimes; Hovikoski et al., 2023). The proximal transition from lower to upper flow regimes represents a rapid increase in water flow velocity and depth through a melt season and transition from inefficient distributed flow to the development of an enlarged, water-filled cavity. ~~The boulder size-distribution suggest~~ Boulder size-distributions suggests that this cavity reached a maximum flow space of 1 m (~~Hovikoski et al., 2023~~) (developmental phase 3, Hovikoski et al., 2023). The development of this enlarged cavity/pond and subsequent water pressure drop encourages localised creep closure at the broadest part of the murtoo (developmental phase 4), evidenced by a disappearance of sorted sediment (interpreted as non-deposition rather than erosion), and in some murtoos this is succeeded by compacted interbedded diamicton—indicating ice-bed recoupling (Hovikoski et al., 2023). Meanwhile, closer to the margins of the murtoo body, meltwater flow continues and is routed obliquely towards the tip, forming boulder-rich proto-channels.
110
115
120 These deposits indicate that the ice-bed recoupling at the broadest part of the murtoo coincided with intense and increasingly erosional channelised flow at the murtoo margins. The final stage of murtoo development (developmental phase 5) is commonly represented by the ~~development~~ generation of boulder-rich marginal channels that finalise the triangular shape of the murtoos (Peterson Becher and Johnson, 2021). ~~Finally, murtoo~~ Murtoo deposition is abruptly terminated and marginal channels are abandoned. The ~~final~~ sedimentation within these marginal channels is characterised by suspension settling and laminated

125 muds, indicating that the depositional space (0.6–0.8 m tall) remained open and water filled but no longer hydraulically connected to the active meltwater system (Ojala et al., 2022; Hovikoski et al., 2023).

130 Importantly, murtoo morphometry (Mäkinen et al., 2017; Ojala et al., 2021), their sedimentological architecture (Peterson Becher and Johnson, 2021; Hovikoski et al., 2023; Mäkinen et al., 2023), and close spatial association with eskers, ribbed tracts, and putative subglacial lakes (Ojala et al., 2021; Ahokangas et al., 2021; Vérité et al., 2022; Mäkinen et al., 2023) suggests that murtoos represent a transition between distributed and channelised drainage. Their formation occurs within broad and low conduits, subject to increasing water discharge throughout a melt season, at water pressures close to or exceeding ice overburden pressure, and with short sediment transport distances such as might be found at the spatial onset of channelisation in a ‘semi-distributed’ transitional drainage system (Hovikoski et al., 2023).

3 Study area

135 Our study area comprises the Finnish Lake District Ice-Lobe (FLDIL, Putkinen et al., 2017; Palmu et al., 2021), central Finland (Figure 1A). The FLDIL is one ice lobe amongst several which comprised the eastern margin of the FIS, and contains the highest density of murtoo fields in the region (Figure 1A, Ahokangas et al., 2021). Murtoo distribution within the FLDIL is representative of their distribution across the wider FIS. In the upstream FLDIL trunk, murtoo fields occur amongst ribbed and hummocky moraines (Figure 1C) in two longitudinal bands, each bounded by a dense assemblage of streamlined forms.

140 In the northeastern longitudinal bands, eskers are particularly clearly associated with murtoo routes (Figure 1D). Downstream, where the FLDIL broadens into a lobe (Figure 1A), murtoo distribution is more fragmented with less clustering evident. Murtoos are sparse in the centre of the ice lobe, ~~however, the area's where~~ thin sediment cover (Figure A1) may ~~limit have limited~~ the material necessary for murtoo formation, and the high density of water bodies may act to mask existing murtoo fields (Ahokangas et al., 2021). The FLDIL geology is predominantly crystalline bedrock, dominated by Precambrian schists, 145 gneisses, and granitoids (Lehtinen et al., 2005) with a thin Quaternary overburden (Lunkka et al., 2021).

In total, the FLDIL encompasses an area of \sim 57,600 km² and its distal margin is clearly defined by the first and second Salpausselkäs (Figure 1A). These large ice-marginal complexes mark the Younger Dryas extent of the FIS (12.7 to 11.7 cal. ka, Donner, 2010; Lunkka et al., 2021). Upstream of the Salpausselkäs there is no clearly defined ice marginal complexes suggesting the FLDIL collapsed continuously and rapidly following the Younger Dryas (Kleman et al., 1997), retreating northwest 150 towards the Scandes mountains (Sweden and Norway) and ice-free by 9–10 cal. ka (Hughes et al., 2016; Stroeven et al., 2016; Regnell et al., 2019). Accordingly, to avoid arbitrarily demarcating an ice margin, we bound our model domain at the second Salpausselkä, which marks the FLDIL extent at \sim 12 cal. ka (Putkinen et al., 2017). With a fixed domain bound at the second Salpausselkä, we are effectively representing a single time slice \sim 12 cal. ka. Shoreline data indicates that the second Salpausselkä terminated in a shallow water body ranging in depth from <5 m to \sim 50 m (Lunkka and Erikkilä, 2012). The 155 speed of the FLDIL retreat, together with the complex and dense assemblage of glaciofluvial landforms (see Palmu et al., 2021; Dewald et al., 2021), suggest that during deglaciation, our study area was characterised by high and spatially extensive atmospheric-driven surface melting delivered to the bed, proximal to significant calving of the FIS into the Baltic Sea Basin

(Greenwood et al., 2017; Patton et al., 2017; Boswell et al., 2019). Conditions within the FLDIL, and the FIS more broadly, were likely comparable to conditions prevalent in land- or shallow-water terminating portions of the Greenland Ice Sheet today
160 (Greenwood et al., 2016; Ojala et al., 2019).

4 Methods

To explore how well a process-based model of basal hydrology can explain murtoo genesis, we applied the Glacier Drainage System Model, GlaDS (Werder et al., 2013), to our study area in the FLDIL. With a representative ice sheet surface and palaeo basal topography, together with a baseline set of GlaDS parameters derived from previous work beneath contemporary ice
165 sheets (e.g., Dow et al., 2018a, 2020, 2022), we compared model output from GlaDS to the subglacial hydrological conditions proposed for murtoo genesis. Model output includes water pressure expressed as a percentage of ice overburden, *overburden%*, sheet discharge, q_s , channel discharge, Q_c , and water velocity, V_W . ~~Spatially, we examined whether GlaDS predicted an area of the bed where overburden $\approx 100\%$, comparing this to the predicted location of murtoo formation 40–60 km from the ice margin, at the upglacier limit of channelisation (Ahokangas et al., 2021; Ojala et al., 2021). We then compared these channels against esker deposits mapped by Palmu et al. (2021). Through time~~ We examined catchment-scale hydrology outputs and compare these to murtoo formation predictions as well as the distribution of channelised landforms (eskers) in the FLDIL. At individual nodes, we compared the evolution of nodes across our domain against the developmental phases recorded within murtoo sediment excavations (see Table 1, Hovikoski et al., 2023). We then explored seasonal and inter-annual model outputs in the area 40–60 km from the ice margin, at the upglacier limit of channelisation, where murtoos are hypothesised to form
175 (Ahokangas et al., 2021; Ojala et al., 2021). Finally, we go on to investigate differences in model outputs between observed murtoo and meltwater routes, and terrain in which there are no glaciofluvial landforms. We sensitivity tested the robustness of all these findings to a range of input parameters. Readers interested in specific details regarding our modelling approaches are referred to Sections 4.1–4.1.2 in which we describe GlaDS; our climate forcing and ice sheet/bed topography; model parameters; and sensitivity testing in detail.

180 4.1 Model description

We used the Ice-sheet and Sea-Level System Model (ISSM, Larour et al., 2012, Revision 27448) and the implementation of the GlaDS model (Werder et al., 2013) contained therein. The GlaDS model (described further in Appendix A and in full in Werder et al., 2013) is a 2D finite element model, which has been widely applied to contemporary ice sheets in Greenland (e.g., Dow et al., 2018a; Cook et al., 2020, 2022; Ehrenfeucht et al., 2023) and Antarctica (e.g., Dow et al., 2018b, 2020; Indrigo et al.,
185 2021; Dow et al., 2022; McArthur et al., 2023; Hayden and Dow, 2023) as well as glaciers in Svalbard (e.g., Scholzen et al., 2021). The GlaDS model operates on an unstructured mesh and includes a model of distributed flow through linked cavities (Hewitt, 2011) represented by a continuous ‘sheet’ of water with variable thickness at mesh elements, and channelised flow—describing ~~uniform~~, semi-circular Röthlisberger channels (R-channels) that are allowed to change diameter—along element edges (Schoof, 2010). Sheet elements exchange water with channels, and the cross-sectional area of these channels evolves

Table 1. Murtoo developmental phases (see Figure 10 in Hovikoski et al., 2023), their sedimentological signature, and anticipated model outcomes, where q_s is sheet discharge ($\text{m}^2 \text{s}^{-1}$), Q_c is channel discharge ($\text{m}^3 \text{s}^{-1}$), $overburden\%$ is water pressure expressed as a percentage of ice overburden pressure, and V_W is water velocity (m s^{-1}). See Section 4.1 and Appendix A for the model description.

Murtoo developmental phase	Sedimentological evidence and interpretation	Expected model outcomes
1	Sorted sediment core within rapidly enlarging cavity, partial ice contact	Sharp increases in q_s , increase in $overburden\%$
2	Onset of spring melt, cavity continuing to enlarge, with deposition of sinusoidal stratification and cobbles	Peak in $overburden\%$, continued increase in Q_c
3	Increasing grain size indicates high water velocity and boulder deposition indicates maximum cavity size of 1 m	Peak in V_W , drop in $overburden\%$, peak in Q_c approaching $1 \text{ m}^3 \text{s}^{-1}$
4	Enlarged cavity leads to water pressure drop and ice-bed recoupling	Continued drop in $overburden\%$ and Q_c
5	Abrupt termination of discharge with appearance of laminated mud	$overburden\%$ approaching winter values

190 through time due to the dissipation of potential energy, sensible heat exchange, and cavity closure rates due to viscous ice creep. Here, flow in both the sheet and channel is assumed to be fully turbulent (cf., Hill et al., 2023). Unlike in other models previously applied to the palaeo setting, GlaDS does not require a predetermined drainage system, the growth and restriction of channels is entirely due to drainage dynamics (Dow et al., 2020). Following Werder et al. (2013), we set a threshold discharge of $Q_c = 1 \text{ m}^3 \text{s}^{-1}$ above which an element edge is classified as a ‘meaningful’ channel for our subsequent analysis.

195 **4.1.1 Model setup: boundary conditions and forcings**

As model inputs, GlaDS requires bed elevation, z_b , ice thickness, H , basal velocity, U_b , boundary conditions, and meltwater input. We anticipate that the modern topography is not representative of bed elevation ~ 12 cal. ka. Therefore, as the baseline z_b , we account for these anticipated changes, particularly in terrain associated with the second Salpausselkä ice-marginal formation, by subtracting Quaternary sediment thickness estimates (GTK, Finland, 2010) from the 25 m/pixel EU-Digital 200 Elevation Model V1.1 (available at: <https://www.eea.europa.eu/data-and-maps/data/copernicus-land-monitoring-service-e-u-dem>). Lake bathymetry was only partially available in the FLDIL, so we did not subtract this from our input DEM in the baseline model. We also did not adjust our model to account for differences in elevation due to glacial isostatic adjustment (GIA) since ~ 12 cal. ka. To ensure the numerical stability of GlaDS the input DEM was smoothed using a low-pass filter. Finally, within steep terrain, an anisotropic mesh ($n_{nodes} \approx 19,000$) was refined based on z_b such that element edges were 205 shortest (to a minimum edge length of 400 m) in rougher terrain and longer where terrain was flatter (to a maximum edge length of 2 km).

We generated H using the 2D Shallow-Shelf Approximation (SSA, MacAyeal, 1989) within ISSM (Larour et al., 2012). An initial estimate of H was given using a parabolic profile as a function of distance from the terminus, and initialisation values for basal velocity were calculated using a stress balance solution for this ice surface. Dirichlet conditions were imposed at the 210 mesh edges along the boundary with zero inflow. Basal motion was modelled using a viscous sliding law (Budd et al., 1979) and following Åkesson et al. (2018) we used a spatially variable basal drag coefficient, a , proportional to z_b , given by:

$$a = 120 \frac{\min(\max(0, z_b + 800), 2000)}{2000}. \quad (1)$$

Ice was assumed to be isothermal with a viscosity, B , equivalent to an ice temperature of -5°C (from Cuffey and Paterson, 2010, p.73; rate factor, A , listed in Table A1). In reality, ice temperature is both spatially and temporally variable. However, 215 without using a more detailed thermomechanical ice model, we follow the previous ad-hoc assumptions of Nick et al. (2013) for the Greenland Ice Sheet and Åkesson et al. (2018) for the FIS, by setting our ice temperature to -5°C . The 12 cal. ka climate for the ice sheet model was estimated using a modern (1981-2010) reanalysis dataset (see Abatzoglou et al., 2018). Precipitation was kept at the contemporary monthly value, but we depressed monthly temperature by 15°C , approximately the temperature 220 differential indicated by NGRIP $\delta^{18}\text{O}$ records (Johnsen et al., 1997). To calculate surface mass balance efficiently in our long term ice sheet model we used a simple positive degree day (PDD) model (as in Cuzzone et al., 2019) allowed to vary about a fixed Gaussian distribution with standard deviation, $\sigma_{PDD} = 5.5^{\circ}\text{C}$ around the monthly mean and a lapse rate of $7.5^{\circ}\text{C km}^{-1}$. To reach volumetric steady state, defined for our ice sheet model as differences in ice volume between successive iterations of less than 10^{-6} km^3 , we ran the ice sheet model for 20,000 years with an adaptive timestep, allowed to vary between 1 day and 1 year. The final H was stored and used as the ice sheet input to GlaDS.

225 As boundary conditions for GlaDS, we imposed a zero flux condition on the domain edge everywhere except at the ice terminus, where given spatial variability in water depth (Lunkka and Erikkilä, 2012), an outlet Dirichlet condition equivalent to atmospheric pressure was prescribed in the baseline model. By enforcing zero input flux we neglect to include basal water input from beyond the model domain and we also do not account for any exchange of water between adjacent ice lobe provinces. To promote model stability, we used an adaptive timestep that was allowed to vary between one hour and ~ 90 seconds and 230 all of our transient models were run for 10,000 days, or ~ 27 years. To approximate winter conditions and avoid suddenly overwhelming our initial system with sudden surface meltwater inputs, we first ran GlaDS to steady state with basal meltwater input but no surface melt. To guarantee the majority of elements were pressurised at the end of each steady state run, we used a low, fixed basal velocity of 30 m yr^{-1} to limit the rate of cavity expansion (see Equation A3). We judged the system to be in steady state once the median difference in sheet thickness between two successive steps was less than 10^{-6} m . This occurred 235 within 20,000 days in all runs, and the majority of nodes reached 90% of overburden pressure ¹ with no channel formation.

For the subsequent transient model runs, melt input to GlaDS was estimated using the same depressed MAT monthly average temperature and precipitation record as with the ice sheet model. In simply depressing the climate by 15°C we do not represent

¹Borehole measurements of overwinter water pressure in the distributed drainage system have been measured at 80-90% of overburden pressure (e.g., Harper et al., 2021)

the complex seasonality (short, warm summers with extreme winters) that characterised the Younger Dryas cold reversal in Fennoscandia (Schenk et al., 2018; Amon et al., 2022). However in fixing our domain to the second Salpausselkä our hydrology 240 model is representative of the end of the Younger Dryas (~ 12 cal. ka) at which time this complex seasonality rapidly gave way to a markedly warmer climate with similar seasonality to the present day (Mangerud et al., 2023). Compared to the ice sheet model, we did use a modified PDD scheme for GlaDS to more faithfully reflect daily temperature variability over the shorter maximum timestep. It is commonly assumed that the total monthly positive degree days can be represented by a fixed Gaussian 245 distribution with $\sigma_{PDD} \approx 5.5^\circ\text{C}$ (e.g., Braithwaite and Olesen, 1989). However, field measurements suggest that this does not hold for the Greenland Ice Sheet (Wake and Marshall, 2015), particularly at temperatures $\geq -5^\circ\text{C}$. Instead, Wake and Marshall (2015) suggest monthly variability in temperature, σ_M , is more accurately described by a quadratic function:

$$\sigma_M = -0.0042T_M^2 - 0.3T_M + 2.64, \quad (2)$$

where T_M is the mean monthly temperature. This function accounts for the reduction in variability with increasing temperature (Gardner et al., 2009; Marshall and Sharp, 2009; Fausto et al., 2011) due to heat buffering, which promotes a more stable 250 boundary layer (Wake and Marshall, 2015). We used σ_M from Wake and Marshall (2015) but did not take into account variations in kurtosis and skewness with temperature, as these become significant where $T_M < -20^\circ\text{C}$ (see Wake and Marshall, 2015), temperatures below those derived from our depressed MAT. Instead we used the calculated σ_M to add Gaussian noise to a daily temperature record estimated by linearly interpolating our depressed MAT record. The number of positive degree days per month, PDD_M was taken as $PDD_M \geq -5^\circ\text{C}$. Following van den Broeke et al. (2010) we used -5°C as our threshold 255 (rather than the more commonly used 0°C threshold) to account for melt which may occur even for days with an average temperature of 0°C . Finally, we used melt rate factors $\gamma_{ice} = 17.22\text{ mm per PDD}$ and $\gamma_{snow} = 2.65\text{ mm per PDD}$ following Cuzzone et al. (2019) keeping these consistent between our ice sheet model and GlaDS model. **Monthly melt was kept fixed annually for each run** **We did not prescribe any inter-annual variability in average monthly temperature**. Melt varied in absolute terms between individual simulations but the mean melt and standard distribution remained identical throughout.

260 The total monthly melt was **converted to yearly melt rates and** routed to the bed via a series of moulins. Following Werder et al. (2013) we divided our domain using Voronoi tessellation on a randomly distributed series of points. Within each Voronoi cell, acting as a ‘catchment zone’, the lowest elevation node was identified and used as the location for a moulin towards which all melt from all other catchment nodes flow. Surface melt rate was integrated over each catchment and converted to instantaneous moulin discharge, Q_m^k . Without a detailed record of daily melt variability we neglect to include daily and diurnal 265 changes in melt, which are known to drive rapid changes in hydraulic head on the Greenland Ice Sheet (Andrews et al., 2014). Smoothing melt variability reduced model size and improved the stability of GlaDS over the ~ 27 year model runs, and we note that the inclusion of an englacial storage term in GlaDS acts to restrict the influence of diurnal variability to within 2 km of moulins with a limited influence on the overall pattern of channelised drainage (see Werder et al., 2013).

4.1.2 Model parameters in the baseline model and sensitivity testing

270 The GlaDS model has been extensively sensitivity tested for contemporary ice sheets where model results can be compared with geophysical evidence to determine the most plausible model output (e.g., Werder et al., 2013; Dow et al., 2018b, 2020, 2022; Indrigo et al., 2021; Scholzen et al., 2021), and as such we do not conduct a detailed review here. We set the parameters in our baseline model (default values listed in Table A1) following the default values in these studies, which provide a reasonable approximation of contemporary ice sheet subglacial conditions. However, because several parameters in GlaDS have uncertain 275 physical values, we did test the robustness of our findings from the baseline scenario throughout the ranges indicated in Table A1. We sensitivity tested for basal melt rate; moulin density and distribution; sheet and channel conductivity terms; basal bump height; the englacial void ratio; basal ice velocity; terminus boundary conditions; bed topography; and mesh geometry. We can assign higher confidence to our baseline model when similar model outputs (e.g., similar channel lengths or patterns of water pressure) are evident across multiple sensitivity tests (e.g., Dow, 2023).

280 Given uncertainty regarding the spatial variability of basal melt rates beneath current and former ice sheets, which vary as a function of geothermal heat and frictional heating, we used a spatially and temporally constant basal water input (as in Dow et al., 2018a, c, 2020; Poinar et al., 2019). Basal melt rates beneath the Greenland Ice Sheet typically range between 1–7 $\times 10^{-3}$ m yr $^{-1}$ (see Karlsson et al., 2021) and we used 5 $\times 10^{-3}$ m yr $^{-1}$ for our baseline model configuration and the majority of the subsequent transient runs. We tested the influence of basal melt rate by running a low basal melt rate (1 $\times 10^{-3}$ m yr $^{-1}$) 285 and high basal melt rate scenario (7 $\times 10^{-3}$ m yr $^{-1}$).

290 As default, surface meltwater was routed through \sim 2500 moulin, a density of 0.04 moulin per km 2 . Measured moulin density varies between 0.02 to 0.09 moulin per km 2 in Greenland (Yang and Smith, 2016). To test the sensitivity of our system to moulin density we also ran models with \sim 1000 (0.02 per km 2), \sim 4000 (0.06 per km 2), and two further randomly generated configurations of the default \sim 2500 (0.04 per km 2). We also tested an additional configuration in which melt at every node was routed directly to the bed.

295 Further sensitivity testing (parameters listed in bold in Table A1) was carried out for several poorly constrained parameters in GlaDS, as well as for the basal geometry and moulin density. The conductivity of both the sheet, k_s and channels, k_c are key controls on the pressure of the system, and alter the relative efficiency of each system, and in turn alter the spacing, length, and upstream pressure influence of channels. The conductivity terms in GlaDS are poorly constrained, and following previous work we tested at magnitude limits up to the point at which the model failed to converge (see Dow, 2023). The baseline value for k_s was 10 $^{-4}$ m $^{7/4}$ kg $^{-1/2}$, and we tested additional setups where $k_s = 10^{-2}, 10^{-3}$, and 10 $^{-5}$ m $^{7/4}$ kg $^{-1/2}$. For k_c the baseline value was 10 $^{-1}$ and we tested $k_c = 5 \times 10^{-1}, 5 \times 10^{-2}$, and 10 $^{-3}$ m $^{3/2}$ kg $^{-1/2}$.

300 The basal bump height, h_r alters how readily cavities open in the distributed system. Our default value for h_r was 0.085 m and we additionally tested $h_r = 0.05$ and 0.1 m. We tested values of englacial storage, $E_{vr} = 10^{-3}$ and $E_{vr} = 10^{-5}$. For basal velocity, U_b , we tested prescribed values of between 100–200 m yr $^{-1}$ chosen to be comparable to surface velocity across land-terminating sectors of the Greenland Ice Sheet (e.g., Tedstone et al., 2015). We tested both a temporally fixed and temporally variable U_b , with the transient U_b varying between 85% and 140% of the mean to approximate speed-ups at the onset of

the melt season and winter slowdowns commonly observed in Greenland (e.g., Sole et al., 2013). Without a more detailed understanding of past ice dynamics, U_b was kept spatially uniform throughout.

305 Although the default configuration describes a terrestrial margin, we also tested the influence of a shallow body of water at the ice margin by prescribing Dirichlet conditions at the ice margin where water pressure is equivalent to that of a uniform 30 m water depth (a simplification of the variable 5–50 m water depth from Lunkka and Erikkilä, 2012). To explore the influence of our modified topography boundary condition, we ran tests with a uniformly flat bed, one representing contemporary terrain (without Quaternary sediment thickness removed), and one with the available partial lake bathymetry removed. Finally, we also
310 explored the dependency of our results on mesh geometry, including using a coarser mesh (maximum edge length of 5 km), a mesh not refined by elevation in any way, and a mesh in which a coarse mesh (edge length between 5–8 km) was prescribed
>>80 km from the ice margin and a much finer mesh (edge length \approx 300 m) was prescribed <80 km from the ice margin.

5 Results and discussion

In total, 30 simulations were carried out and for each model run, we examined the subglacial water pressure, expressed as a
315 percentage of the overburden pressure, $overburden\%$, sheet discharge, q_s on element faces; channel discharge Q_c on element edges, and water velocity, V_W . In order to examine how well GlaDS is able to explain murtoo genesis we first describe the catchment scale hydrology across our model runs and examine the evolution of the model through time (Sections 5.1–5.3). In Section 5.4 we describe the limitations of our approach and suggest possible future research.

5.1 Catchment scale hydrology

320 In the baseline model (see Figures 2, & 3), model outcomes at the catchment scale suggest that GlaDS matches several of the spatial predictions for murtoo genesis. After an initial adjustment from steady state to transient forcing over five years, the baseline model reached a quasi-steady state configuration in which the system responded seasonally to summer meltwater input (Figure A3). Following this adjustment, a clear and sharply demarcated transition in drainage modes develops ~~between~~
40–60 km from the ice margin during summer. Murtoos are predicted to have formed at this distance from the ice margin of the
325 FIS, as widespread distributed drainage gave way to channelised drainage within a semi-distributed system (see Mäkinen et al., 2017, 2023; Peterson Becher and Johnson, 2021; Ojala et al., 2019, 2021, 2022; Ahokangas et al., 2021; Vérité et al., 2022; Hovikoski et al., 2023). Additionally, weak to moderate deformation of murtoo sediments suggests that water pressure remained at or close to overburden pressure for sustained periods during the melt season (Peterson Becher and Johnson, 2021; Vérité et al., 2022; Mäkinen et al., 2023; Hovikoski et al., 2023). In our results, a persistent area of $overburden\% > 100\%$ develops
330 across the full width of the domain 40–60 km from the ice margin during summer (Figures 2,3, & Movie A1). Outside this area (<40 km of the ice margin, and >70 km from the ice margin) $overburden\%$ is 10–30% lower during summer. By winter, $overburden\%$ drops by up to 30% across the domain as melt ceases (Figure 2A).

Approximately 35 modelled channels (edges where $Q_c > 1 \text{ m}^3 \text{ s}^{-1}$) extend up to 50 km perpendicular from the ice margin, into but not beyond the hypothesised zone of murtoo formation (Ojala et al., 2021) and terminate where $overburden\%$

335 exceeds 100% during summer. Murtoo fields (Ahokangas et al., 2021) are evident at the head of many modelled channels, particularly in the western and eastern areas of the ice-lobe (Figure 4A). Within 40–60 km of the ice margin, the median cross-sectional area of edges is 2.8 m^2 (equivalent to a semi-circle with radius of 1.3 m). Closer to the ice margin, the median summer Q_c of channels reaches up to $100 \text{ m}^3 \text{ s}^{-1}$ (Figure 2D) and they are comparable in both sinuosity and spacing to esker deposits in the FLDIL (Figure 4, Palmu et al., 2021). Channel spacing and length is also comparable to the theoretical 340 spacing of eskers derived from the modelling results of Boulton et al. (2009) and Hewitt (2011). The development of channels during summer also strongly influences q_s and V_W , and each ~~peak-are highest~~ adjacent to active channels close to the ice margin ($q_s \approx 10^{-3} \text{ m}^2 \text{ s}^{-1}$, $W_V \approx 1.4 \times 10^{-3} V_W \approx 1.4 \times 10^{-3} \text{ m s}^{-1}$), and remain high until 40–60 km from the ice margin ($q_s \approx 10^{-4} \text{ m}^2 \text{ s}^{-1}$, $W_V \approx 8 \times 10^{-4} V_W \approx 8 \times 10^{-4} \text{ m s}^{-1}$) where values drop to ~~to~~ a low upglacier ($q_s \approx 10^{-5} \text{ m}^2 \text{ s}^{-1}$, $W_V \approx 1 \times 10^{-4} V_W \approx 1 \times 10^{-4} \text{ m s}^{-1}$).

345 Without ~~observational-independent~~ constraint against which to compare our results, we ran additional sensitivity tests to explore the parameter dependency of our findings, assigning higher confidence to model outcomes present across the majority of tests (see Dow, 2023, and section 4.1.2). The catchment scale hydrology described in our baseline model remains consistent across most of the additional sensitivity tests~~and continue to align well with the~~. ~~Furthermore, sensitivity test results remain consistent with~~ predictions for murtoo genesis. This includes for: all moulin density tests (Figures A10, & A12–A14), except 350 the highest moulin density; ~~variable~~ basal melt rate (Figures A15, & A16); ~~modified~~ mesh geometry and bed elevation (Figures A23–A22); the addition of lake bathymetry (Figure A24); a shallow proglacial water body (Figure A25); ~~differences in~~ the englacial void ratio (Figures A26–A27); and basal velocity (Figures A28–A32).

355 While catchment-scale trends are largely robust, the exact location of channels, and their exact length and local *overburden%*, does vary between sensitivity tests. Because GlaDS operates on a fixed mesh (cf. Felden et al., 2023), the resolution of which is a balance of suitable fidelity against the increased computational cost of resolving finer details, the exact location of ~~modelled channels where channels may form~~ does vary between sensitivity tests. These minor differences in ~~channels~~ channel location 360 change the spatial expression of summer *overburden%*, with the area of *overburden%* $\approx 100\%$ changing by up 10 km and differences of between 5–10% for any given location. Channel location is particularly sensitive to mesh geometry, but differences also arise because of moulin density and location, bed topography, basal velocity, and basal bump height. However, while the absolute position of channels does vary, channel spacing remains consistent (~ 15 km), and changes in channel length are limited to a maximum of ~ 10 km.

365 ~~Channel~~ Although consistent across the majority of tests, ~~channel~~ length and *overburden%* does vary considerably ~~in six of our sensitivity tests. As reported elsewhere (e.g., Werder et al., 2013), GlaDS is most sensitive to changes in the~~ at the tested limits of k_s and k_c parameters, describing the sheet and channel conductivity respectively. ~~At~~ (Werder et al., 2013). For both the maximum tested sheet conductivity ($k_s = 10^{-2} \text{ m}^{7/4} \text{ kg}^{-1/2}$, Figure A4) and the minimum tested channel conductivity ($k_c = 10^{-3} \text{ m}^{3/2} \text{ kg}^{-1/2}$, Figure A9), there are major changes to the catchment hydrology. Channels are restricted to within ~ 1 km of the ice boundary and *overburden%* within and near to these channels is $\approx 50\%$ when $k_s = 10^{-2} \text{ m}^{7/4} \text{ kg}^{-1/2}$ and approaches 120% when $k_c = 10^{-3} \text{ m}^{3/2} \text{ kg}^{-1/2}$.

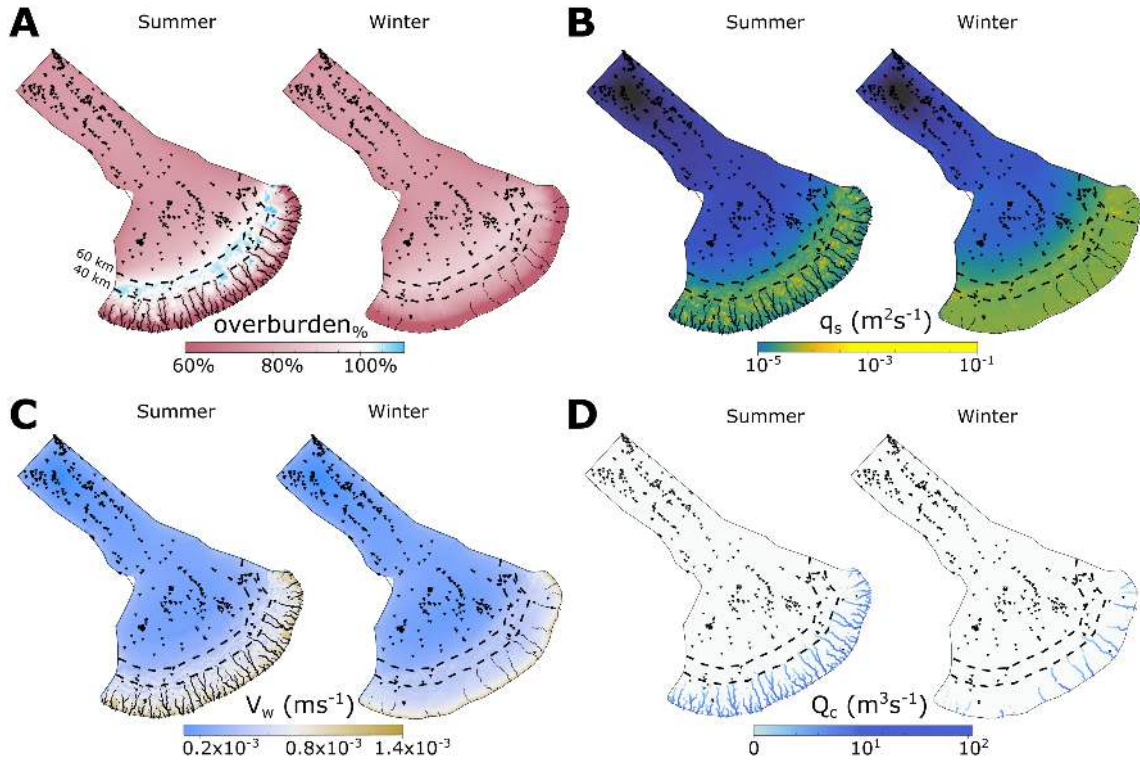


Figure 2. Median summer and winter system states in the baseline model run. **A)** Water pressure as a percentage of overburden pressure, *overburden%*. In summer and winter, **B)** Sheet discharge, q_s . **C)** Water velocity, V_w . **D)** Channel discharge, Q_c . For each output, we took the median from model years 5–27 disregarding the initial period of adjustment to transient forcing. *Summer* extends from May to September, all other points fall into *winter*. Note that the scales for panels B and D are logarithmic. Dashed lines in all panels indicate contours of 40 and 60 km from the ice margin. Murto fields (Ahokangas et al., 2021) are shown as inverted triangles in all plots. Channels are shown as black solid lines in panels A–C.

At For both the minimum sheet conductivity ($k_s = 10^{-5} \text{ m}^{7/4} \text{ kg}^{-1/2}$, Figure A6) and the maximum channel conductivity 370 ($k_c = 5 \times 10^{-1} \text{ m}^{3/2} \text{ kg}^{-1/2}$, Figure A7) channel length increases to between 50–60 km, only a 10 km increase in channel length compared to the baseline scenario, but there are additional major changes in *overburden%*. At the minimum k_s , an area of *overburden% ≈ 100%* extends up to 150 km from the ice margin during summer, and at the maximum k_c there is no area of *overburden% > 90%* during summer. When $k_s = 10^{-3} \text{ m}^{7/4} \text{ kg}^{-1/2}$ (Figure A5) and when moulin density is highest (Figure A11), channels are restricted to within 20 km and there is an area of high *overburden% > 100%* between 10–70 km of 375 the ice margin.

Changing the channel and sheet conductivity by orders of magnitude strongly modifies the efficiency with which either the distributed or channelised system can transmit water, limiting the influence of the other system (Werder et al., 2013). At the highest tested moulin density, the reduced discharge associated with any one moulin resulted in a higher density of short

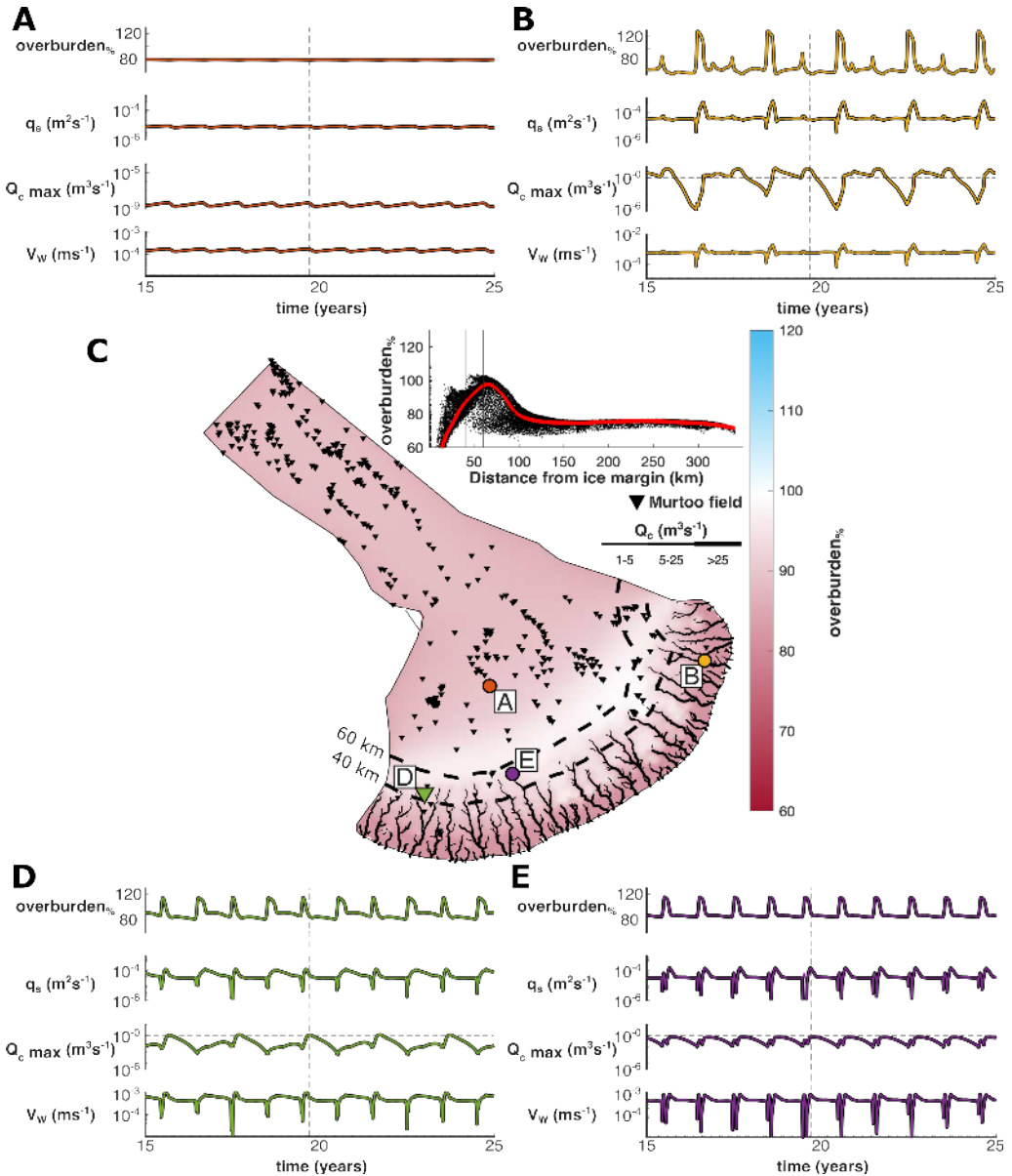


Figure 3. The evolution of water pressure as a percentage of overburden pressure, ($overburden\%$), sheet discharge, (q_s), water velocity, (V_W), and maximum channel discharge, (Q_{cmax}) at four nodes over model years 15–25 in the baseline model run. **A)** Node No. 6,277 located \sim 120 km from the ice margin. **B)** Node No. 18,517 located \sim 17 km from the ice margin. **C)** Overburden at the end of the melt season in model year 19 (arbitrarily selected). Channels are represented as black lines, murtoo fields as inverted black triangles, and the location of panels A, B, D, and E as coloured points. Inset shows overburden at every node as a function of distance, D from the ice margin with a smoothing function shown in red and vertical lines at 40 and 60 km from the ice margin. **D)** Node No. 16,402 located 0.7 km from a murtoo field and \sim 45 km from the ice margin. **E)** Node No. 3,842 located \sim 54 km from the ice margin at the head of a channel system without an adjacent murtoo field. The time slice shown in panel C is represented as a vertical dashed line in panels A, B, D, and E. Note the logarithmic scale for q_s and Q_{cmax} .

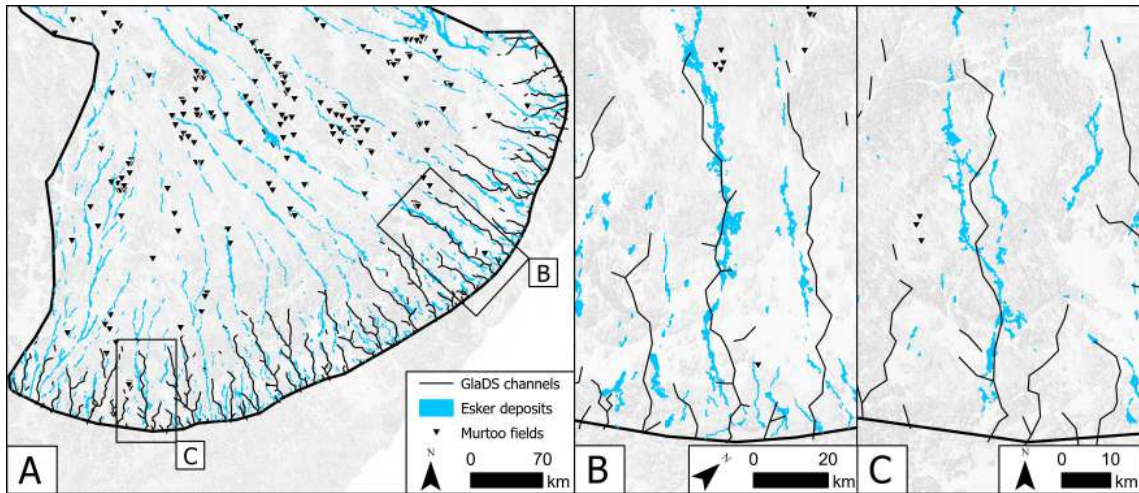


Figure 4. Modelled channel location compared to esker deposits (mapped by Palmu et al., 2021) and murto fields (mapped by Ahokangas et al., 2021) at the ice margin of the FLDIL. **A)** Modelled channels during summer in the baseline run (black lines) across the full width of the domain compared to esker deposits (blue polygons) and murto fields (inverted black triangles). Each channel is defined where the median channel discharge, Q_c , exceeds $1 \text{ m}^3 \text{ s}^{-1}$ during summer. **B & C)** Detailed comparison of two large esker systems against model channels.

channels as fewer reach the threshold discharge at which wall-melt exceeds creep-driven channel closure. Excessively long (380) ($>50 \text{ km}$) or short ($<10 \text{ km}$) channels ~~compared to the majority of tests, as well as to contemporary channels in Greenland (e.g., Chandler et al., 2013; Dow et al., 2015), together with major changes in system pressure at the tested limits of k_s and k_c suggest are considered to be invalid on the basis of modern Greenland observations (e.g., Chandler et al., 2013; Dow et al., 2015) and an anomalous overburden%~~ is considered invalid on the basis of the conceptual model for murto distribution and genesis (e.g., Ahokangas et al., 2021; Hovikoski et al., 2023). Therefore, our baseline conductivity terms are the ~~considered the most~~ 385 plausible parameters.

Finally, given the parameters in our baseline model are set following existing work on contemporary ice sheets (Section 4.1.2), it is no surprise that at the catchment scale, the modelling outputs appear similar to the subglacial hydrological system evident in land-terminating sectors of the Greenland Ice Sheet. Tracer transit times (e.g., Chandler et al., 2013) and basal hydrology modelling indicate efficient channelisation extends up to 40–50 km from the ice margin in Greenland, transitioning between channelised and distributed drainage modes where ice is $\sim 900\text{--}1200 \text{ m}$ thick (De Fleurian et al., 2016; Dow et al., 2015) as it does here. However, the pressure conditions within large channels close to the ice margin ~~is~~are notably different in our model results compared to the Greenland settings (e.g., Van de Wal et al., 2015), ~~where~~In Greenland, channels exist at lower water pressures than the surrounding distributed system (Davison et al., 2019)~~–In Greenland, and~~ the resultant hydraulic potential gradient forces large volumes of water from the surrounding distributed system towards channels, in turn 395 lowering water pressure in the distributed system and increasing basal traction (Schoof, 2010). Even as meltwater delivery to

the bed subsequently increases through the melt season, these channels can act to reduce ice velocity (Nienow et al., 2017) and reduce ice mass loss. In contrast, the channels modelled here remain at relatively high *overburden%* throughout the year (> 60%), with a lower hydraulic potential gradient between channelised and distributed systems. The FLDIL is low-relief compared to the steep margins of the Greenland Ice Sheet (e.g., Wright et al., 2016), and the shallow topography may act to reduce the hydraulic gradient between distributed and channelised drainage. As a result, the influence of channelisation on basal velocity would be relatively limited in the ~~FLIDL~~^{FLDIL}. Lower rates of water exchange between distributed and channelised drainage would permit more of the bed to remain closer to $overburden\% \approx 100\%$, sustaining higher velocities for extended periods of time (Dow et al., 2022), highlighting the sensitivity of low-relief areas of the FIS to extensive atmospheric melting.

5.2 Comparison to the murtoo developmental phases

The widespread and time-integrated distribution of murtoos throughout our model domain complicates model validation as murtoo formation conditions remain uncertain. The ability of GlaDS to reproduce the hypothesised spatial pattern of murtoo formation (i.e., summer $overburden\% \approx 100\%$ 40–60 km from the ice margin) alone cannot definitively confirm or refute the hypothesized formation process because murtoos are distributed across our model domain. In this context, comparing seasonal model evolution to murtoo sedimentology (e.g., Hovikoski et al., 2023; Mäkinen et al., 2023) becomes particularly important as there are multiple predictions in sequence that the model must achieve (Table 1).

Examined at individual nodes through time, the baseline model (and most sensitivity tests) agrees well, though not perfectly, with the hypothesised conditions and location of murtoo genesis. Internal murtoo sediments chart an overall increase in meltwater discharge throughout the melt season followed by an abrupt termination (Table 1), possibly within the same year (Hovikoski et al., 2023). Against this backdrop, the alternating sequences of glaciofluvial deposits in the main body of murtoos suggests that the system was also subject to repeated pulses of meltwater and rapid changes in flow regime, marking the rerouting and periodic isolation of cavities within a developing, semi-distributed drainage system (Hovikoski et al., 2023; Mäkinen et al., 2023). Figure 3 shows the evolution of the system through time at four representative nodes across the study area. At node 6,277, 120 km from the ice margin and upglacier of any significant surface melt inputs, the system is effectively inert, with $overburden\%$ remaining $\approx 80\%$ and only small periodic perturbations in q_s , Q_c , and V_W . However, closer to the ice margin, the system responds annually to meltwater inputs and is more variable through time.

Figure 3D & E demonstrates the seasonal evolution of two nodes between 40–60 km from the ice margin, each nearby to channel systems. Both nodes undergo a rapid fall within the hypothesised zone of murtoo formation and both nodes display drainage behaviour which could accommodate murtoo formation, with a seasonal increase in $overburden\%$ up to a maximum of approximately 120 % with and a more gradual decrease thereafter. However, the two nodes show different interannual behaviour, and only one is located close to a murtoo field. At node 3,842, ~54 km from the ice margin and chosen to be representative of surrounding nodes at the onset of a channel (Figure 3E), this pattern the pattern of drainage repeats annually—every year the increase and decrease in $overburden\%$ is accompanied by peaks in q_s , Q_c , and V_W and the nearby development of channels throughout the meltwater season. At the onset of channelisation the maximum Q_c approaches but never exceeds

1 m³ s⁻¹. ~~Although node 3,842 is not located near to a murtoo field, However, although~~ this evolution through time does
430 appear consistent with each of the murtoo developmental phases (Table 1). ~~node 3,842 is not located near to a murtoo field.~~

At node 16,402, located 0.7 km from a murtoo field and chosen to be representative of murtoo fields, a more complex signal is evident. At the maximum upglacier extent of two adjacent channels, ~45 km from the ice margin a biannual signal is evident (Figure 3D). Every year, there is a sharp increase in *overburden%* at the start of the melt season to *overburden%* $\geq 100\%$. However, the subsequent drop in *overburden%* varies every other year. Either *overburden%* spikes and then drops rapidly
435 over 1-2 months to the winter value (~80%) until the following melt season, or the drop in *overburden%* is initially shallower before quickly dropping to an *elevated* *overburden%* (~90%) *that is elevated* relative to the previous winter. Years *in which the drop in with an elevated winter* *overburden% is more gradual* are also associated with lower Q_c and flatter peaks in q_s . In contrast, years that have a rapid drop in *overburden%* after the start of the melt season are associated with higher values
440 of Q_c , approaching 1 m³ s⁻¹ and sharper peaks in q_s . *These odd-numbered years are* *We consider that the latter case is* more consistent with the murtoo developmental phases (Table 1) because the higher values of Q_c indicate discharge approached that necessary to form channels.

A similarly biannual pattern is evident at node 18,517, 17 km from the ice margin and colocated with a channel (e.g., Figure 3B). Here, close to the ice margin the maximum Q_c associated with edges connected to the node exceeds the threshold for a meaningful channel every summer, reaching a peak of 200 m³ s⁻¹ ~June each year with a maximum cross-sectional channel
445 area of 42 m² (equivalent to a half-circle with radius, $r \approx 5$ m). However, every other year, the maximum *maximum* Q_c of edges connected to node 18,517 remains ≥ 1 m³ s⁻¹ i.e., the channel remains active. *As a result, subsequent meltwater input over winter. Preexisting channels dampen the influence of melt in the following summer through these persistent channels is quickly accommodated by providing an already established efficient drainage pathway* with only a small increase in *overburden%* and little change in q_s (Figure 3B). *Channels persist during winter. Overwinter channels form* across the width of the domain in the
450 baseline model, *and but* an alternating spatial pattern of overwinter channel persistence is evident. In any given year, channels will persist through winter in either the central third of the lobe or in the remaining two thirds of the lobe (Figure A2 & Movie A1).

Finally, although individual nodes do track the overall increase in meltwater discharge throughout some melt seasons, as well as the evolution of *overburden%* consistent with limited cavity expansion, our modelling fails to reproduce the sharp
455 drop in discharge at the end of the melt season or the rapidly changing flow regimes within a single melt season *that have been invoked to explain murtoo sedimentology* (see Mäkinen et al., 2023; Hovikoski et al., 2023, and Section 2). We did not include diurnal variability in our modelling on the grounds of model stability and the limited influence diurnal forcing has on catchment scale drainage in GlaDS (Section 4.1.1 & Werder et al., 2013). Diurnal forcing would be critical in order to represent rapid changes in the flow regime within murtoo-forming cavities. However, *GlaDS is also as with other subglacial hydrology models, GlaDS is* a model in which the subglacial system is assumed to be pervasively hydraulically connected
460 (see Rada Giacaman and Schoof, 2023), and there is no mechanism which can lead to the hydraulic isolation of specific areas of the bed (e.g., Rada and Schoof, 2018; Hoffman et al., 2016). As a result, even if diurnal forcing were to be included, we do not expect to be able to reproduce the rapid changes in meltwater discharge necessary to form upper and lower flow regime

deposits (see Section 2, & Hovikoski et al., 2023) or laminated muds in marginal murtoo channels (e.g., Ojala et al., 2022).

465 ~~Including spatially variable system conductivity is likely to be important in future work which seeks to evaluate the ability of process-based subglacial hydrology models to represent landform formation.~~

5.3 Meltwater routing beneath the Finnish Lake District Ice Lobe Comparing murtoo and meltwater route hydrology

Extensive geomorphological mapping has identified meltwater pathways across the FIS and within the FLDIL in particular (see Dewald et al., 2021; Ahokangas et al., 2021). ~~In an effort both to evaluate the ability of GlaDS to represent these~~

470 ~~meltwater pathways, as well as explore the cause of the biannual signal evident at individual nodes, we took~~ ~~We explore drainage behaviour in the area of anticipated murtoo formation by isolating and taking~~ a spatial median of nodes ~~from~~ ~~in~~ the baseline model 40–60 km from the ice margin. We grouped nodes by their relation to i) murtoo routes ($n = 244$), ii) meltwater

475 routes ($n = 951$), and iii) neither ($n = 1205$), using 500 m buffers to approximate the lateral extent of murtoo/meltwater routes along 2D polylines from Ahokangas et al. (2021). Thresholding by distance is necessary to exclude nodes which either

480 i) do not respond seasonally to meltwater input (e.g., those > 60 km from the ice margin, Figure 3A), or ii) nodes closer to the ice margin (within 0–40 km) where channelised drainage dominates in our modelling. Nodes 40–60 km were selected because this is both the hypothesised area of murtoo formation (Ahokangas et al., 2021) and the location in our modelling identified as one in which conditions for murtoo formation are met (Section 5.1). We note that we also include eskers within 40–60 km of the ice margin (mapped as ‘channelised routes’ by Ahokangas et al., 2021) which likely postdate ~ 12 cal. ka.

485 We do not have age-control on any individual landform and many channelised routes intersect or overprint murtoo/meltwater routes (Ahokangas et al., 2021), so we therefore classified them accordingly.

Plotting the median evolution of these groups through time (Figure 5) and as probability density functions (Figure 6) reveals clear differences between nodes in murtoo or meltwater routes and nodes which do not intersect any mapped glaciofluvial geomorphology. Compared to individual nodes (Section 5.2) the average evolution of nodes in murtoo and meltwater routes

485 follows a regular pattern year-on-year (Figure 5). At the onset of the melt season, following winter minima, *overburden%*, q_s , Q_c and V_W all begin to increase (Figure 5). The increase in *overburden*, q_s , and V_W is sharp, with a more gradual increase in Q_c through time. As cavity expansion promotes lower water pressure and more efficient discharge, *overburden%* peaks earliest \sim June each year, but remains $>100\%$ until \sim August, at which point V_W and q_s peak. As *overburden%*, q_s , and V_W all decrease towards winter ~~minimums~~ ~~minima~~ following peak melt, Q_c peaks in September, decreasing steadily towards

490 a minimum before the next melt season. By contrast, the pattern across all other nodes (i.e., those which do not intersect mapped glaciofluvial geomorphology) remains relatively stable through time, and *overburden%*, q_s , Q_c and V_W ~~is~~ ~~are~~ lower throughout the year, suggesting there is limited evolution of the hydrological system in these nodes. ~~In clearly distinguishing murtoo and meltwater routes from nodes which do not intersect mapped glaciofluvial geomorphology, GlaDS appears to be faithfully representing the drainage pathways active beneath the FLDIL at the end of the Younger Dryas ~ 12 cal. ka.~~

495 ~~Although through time~~ ~~The probability density functions of~~ murtoo routes and meltwater routes ~~appear similar, differences between the two are evident. Plotted without respect to time in terms of probability density, the difference between murtoo is also clearly distinct from terrain without glaciofluvial landforms (Figure 6). However, the probability density functions~~

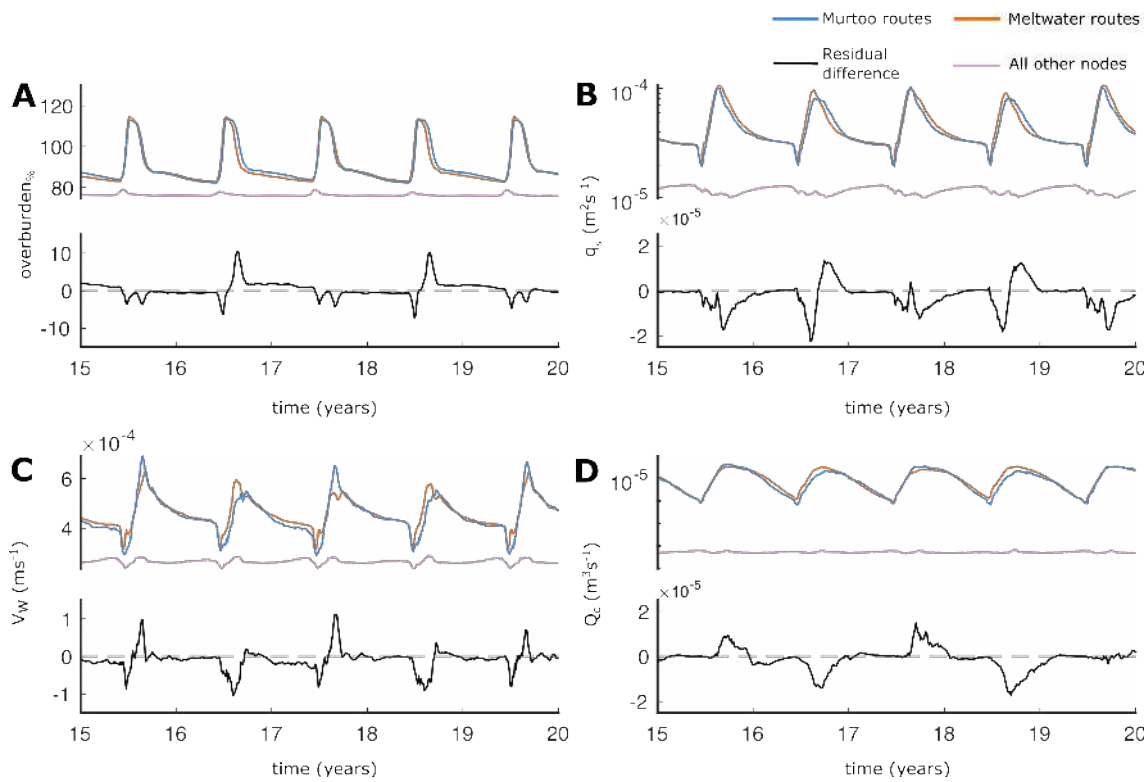


Figure 5. Median output during model years 15–20 at nodes between 40–60 km from the ice margin. In all panels, nodes that fall within murtoo routes are shown in blue, those which fall within meltwater routes (without murtoos) are shown in orange, and all other nodes are shown in purple. The black line in each panel represents the residual difference between the median of murtoo routes and meltwater routes. A positive residual indicates higher median values in murtoo routes, and vice versa for negative residual values. **A)** Water pressure expressed as a percentage of overburden, *overburden%*. **B)** Sheet discharge, q_s . **C)** Water velocity, V_W . **D)** Channel discharge, Q_c . Note panels B and D have logarithmic scales.

of murtoo routes and meltwater routes is clearest—~~are also different from one another, particularly~~ at the lower tail of the distribution distributions (Figure 6). Murtoo routes have a *overburden%* distribution with a more tightly constrained lower tail ~~than meltwater routes~~, with fewer nodes dropping below *overburden% = 80%*~~and a more variable~~. There is a bimodal distribution of both q_s and V_W ~~than meltwater routes~~—~~within murtoo routes that is not evident in meltwater routes at the lower tail of the distribution~~. Both meltwater routes and murtoo routes have a bimodal Q_c distribution, but the lower murtoo route peak is offset towards higher channel discharges. One-way ANOVA testing indicates that ~~this difference~~ the difference in distribution between murtoo and meltwater routes is statistically significant ($p < 0.05$ at the 95% confidence interval). Additional Tukey-Kramer testing indicates that the significant difference between murtoo and meltwater routes varies throughout the year (Tables A2–A5). In June and July, *overburden%* is significantly lower in murtoo routes than in meltwater routes by 1–3%, throughout the rest of the year, *overburden%* is significantly higher in murtoo routes than in meltwater routes by the same

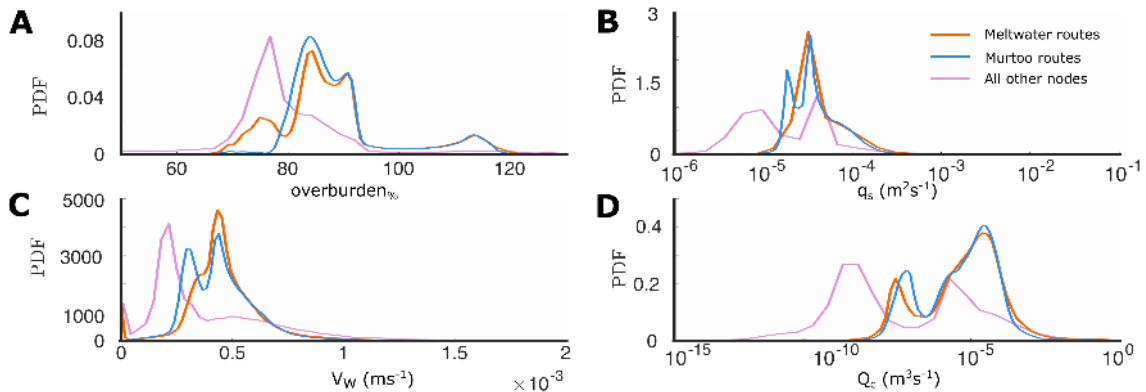


Figure 6. Probability density estimates from kernel smoothing of model output during all model years at nodes between 40–60 km from the ice margin. As in Figure 5, nodes that fall within murto routes are shown in blue, those which fall within meltwater routes (without murtoos) are shown in orange, and all other nodes are shown in purple. **A)** Water pressure expressed as a percentage of overburden, *overburden*%. **B)** Sheet discharge, q_s . **C)** Water velocity, V_W . **D)** Channel discharge, Q_c . Note panels B and D have logarithmic scales.

amount. Between January and May there are no significant differences in q_s between murto routes and meltwater routes. However, between June and December, q_s is significantly lower in murto routes than in meltwater routes by $\sim 1 \times 10^{-5} \text{ m}^2 \text{s}^{-1}$.

510 There are no statistically significant differences in Q_c between murto routes and meltwater routes throughout the year. Statistically significant differences between murto/meltwater routes and all other nodes is limited to between June and October when Q_c is significantly higher in murto and meltwater routes than beyond by $\sim 1 \times 10^{-5} \text{ m}^3 \text{s}^{-1}$. Finally, throughout the year, V_W is higher in murto and meltwater routes than beyond them by $\sim 1 \times 10^{-3} \text{ m s}^{-1}$. In murto routes V_W is significantly lower for each month than in murto free meltwater routes by $\sim 1 \times 10^{-4} \text{ m s}^{-1}$.

515 ~~In clearly distinguishing murto and meltwater routes from nodes which do not intersect glaciofluvial landforms, GlaDS appears to be faithfully representing the drainage pathways active beneath the FLDIL at the end of the Younger Dryas ~ 12 . Further, with a statistically significant difference between murto routes and meltwater routes, our modelling appears to capture subtle differences in the two which may explain the spatial distribution of murtoos within the FLDIL. However, it is difficult to say whether or not these differences are truly the model capturing subtle differences between water flow in meltwater routes and murto routes or if they arise due to our model setup. There is, for an example, a spatial component to the biannual signal in our murto route outputs, potentially~~ The differences between meltwater routes and murto routes are subtle, and the annual evolution of model outputs in both closely match the murto developmental phases (Table 1 & Hovikoski et al., 2023). We anticipate that this statistical difference has a strong spatial component linked to the ~~observation of winter channels persisting after the end of the melt season. Modelled channels do not always coincide with murto fields, particularly within the centre of our domain, overwinter channels reported in Section 5.2—murto routes are notably absent~~ 40–60 km from the ice margin (e.g., node 3,842, Figure 3E). Here, our baseline scenario also reproduces apparent conditions for murto formation, including the termination of low-discharge channels and $\text{overburden} \% \approx 100\%$ over a broad area during summer (e.g., Figure 2 in the centre

520

525

of the FLDIL, whereas meltwater routes are more evenly distributed across the full width of the domain (see Figure A1A). Despite this, no murtoo fields have been mapped in this area (Ahokangas et al., 2021). Winter channels meanwhile follow 530 a pattern in which Murtoo distribution closely overlaps with the distribution of overwinter channels and when channels in the central third of the FLDIL lobe persist in alternating winters to persist over one winter, those in the northernmost and southernmost outer thirds. The presence of these winter channels likely influences the nearby system through the following summer, with preexisting channels dampening the influence of the initial melt input by providing an already outer two thirds 535 do not—and vice versa in the following winter (Figure A2). As a result, when overwinter channels persist nearby to murtoo routes, the following summers are characterised by sharper peaks in *overburden%* and lower values of Q_c , V_W and g_s as melt is quickly accommodated by an established efficient drainage pathway. With an absence of murtoos in the central third of the lobe, the significant biannual (Section 5.2). In contrast, meltwater routes—distributed more evenly—are less sensitive to the spatial pattern of winter channels. We therefore anticipate that the statistically significant difference between murtoo routes and meltwater routes (distributed more evenly across the FLDIL, Figure A1A) may be an artefact of the spatial expression of winter 540 channels. Murtoos appear to form within a semi-distributed drainage environment, and sedimentological studies indicate the movement of sediment is important in murtoo formation (Peterson Becher and Johnson, 2021; Mäkinen et al., 2023; Hovikoski et al., 2023). The reason that murtoos are not present in the centre of the FLDIL where our modelling suggests they should form may be a preservation issue or due to limited sediment supply (e.g., Bradwell, 2013). Sediment cover in this area is very thin, and the large areas of exposed bedrock likely limited the upstream supply of sediment from which murtoos could form (Figure A1B), 545 an interaction not yet accounted for in our modelling. Modern lakes are also abundant in the centre of the FLDIL and these may also act to mask murtoo routes, arises because of the repetitive expression of overwinter channels, and does not necessarily indicate that GlaDS is resolving differences between the landforms themselves.

However, the factors giving rise to the spatial pattern of winter channels themselves are more complex. On the Greenland Ice Sheet, winter slowdowns following high-melt summers have been linked to the sustained persistence of larger and more 550 extensive channels into winter months (Sole et al., 2013) and their existence alone in our baseline model is not necessarily surprising. There is a spatial variability to our meltwater inputs, arising from heterogeneity in the climate reanalysis used to estimate the Younger Dryas climate (Section 4.1.1). However, our fixed repetitive model forcing, though cyclical, has no interannual variability and no melt seasons are any more elevated than others. Additionally, as described in Section 4.1 and following Werder et al. (2013), an arbitrary minimum threshold $Q_c \geq 1$ was defined, above which Q_c along an element edge 555 was classified as a meaningful ‘channel’. Channels persisting through winter months tend to operate at very low discharges of 1–3, and would not be categorised as channels with a higher threshold. Nonetheless, despite their low discharge and our fixed cyclical forcing, these channels do have a discontinuous spatial distribution with a biannual signal, which together with their winter persistence must arise, at least in part, for reasons besides our choice of external climate forcing or our choice of Q_c threshold.

560 The lobate geometry of our model domain, chosen to be representative of the extent of the FLDIL (~12, may control the spatial expression of winter channels in our baseline model. In turn, these winter channels may contribute to the significant difference in the drainage characteristics of murtoo and meltwater routes. The divergence of ice flow vectors within the lobe

appear to act as an initial perturbation which, fixed ice sheet geometry, and constant basal velocity (see Section 4) likely explains their repetitive interannual expression, however the the spatial pattern of overwinter channels is unexpected. The lobate 565 geometry of the ice lobe is one possible explanation, and together with spatial variability in the climate signal, results in an initially input may result in a non-uniform concentration of meltwater within the lobe . We hypothesise that this local concentration of meltwater promotes large enough channels in portions of our model that are able to resist closure during winter, which subsequently act to more efficiently remove meltwater and lead to an earlier peak discharge the following summer, and an earlier closure in the following winter. The repetitive biannual pattern of this signal which is allowed to persist 570 because of fixed model forcing. In a more sophisticated model setup—one including sediment dynamics; coupled ice flow and subglacial hydrology; and/or more realistic meltwater variability—the repetitive pattern of overwinter channels is unlikely to persist in a more realistic model setup subject to more realistic year to year variability in meltwater forcing. Nonetheless, and overwinter channels may be absent altogether. Murtoo route distribution meanwhile appears to be a complex interplay of upstream sediment availability; meltwater input location and timing; local geology; ice velocity; and drainage characteristics 575 (see Ahokangas et al., 2021). By predicting the apparent conditions for murtoo formation where no murtoo routes are present (e.g., in the centre of the divergence of flow beneath the FLDIL is likely to be important in glaciofluvial landform generation. Flow parallel lineations (e.g., Figure 1E) indicate a largely uniform flow direction within the primary trunk that diverges radially within the lobe. As a result, landforms within the FLDIL have previously been divided into three sub-lobes. The boundaries between these three sub-lobes are demarcated by particularly large esker deposits suggesting a concentration of 580 meltwater here (Palmu et al., 2021). These eskers and the sub-lobes they bound align approximately with the distinct alternating pattern of over-winter channel persistence FLDIL, 40–60 km from the ice margin, Figure 3B) it is clear that although GlaDS is capturing the broader patterns of meltwater drainage, it is failing to reproduce the exact spatial pattern of murtoos themselves, likely due to an incomplete description of subglacial processes in our modelling (see Section 5.4). Nonetheless, our results 585 clearly demonstrate the potential for GlaDS to represent subglacial hydrology beneath former ice sheets, but further research is necessary to more accurately resolve the specific spatial distribution of murtoos.

5.4 Limitations and future work

This work represents, to the best of our knowledge, the first comparison of a process based subglacial hydrology model to a 590 specific glaciofluvial landform specific glaciofluvial landforms and we view it as necessarily exploratory. To ensure models could run to completion with wall-time of 1–2 days and remain numerically stable across the tested range of parameters we make a number of simplifying assumptions. These include smoothing of the bed topography below the maximum resolution available, and using a relatively large mesh. However, sensitivity testing indicates our conclusions are largely insensitive to topography, including its absence—a total absence of relief, and that the ice surface gradient instead imposes the dominant 595 control on basal hydrology. Similarly, changing the mesh resolution also appears to have limited impact on our conclusions. We did not account for changes in elevation due to glacial isostatic adjustment (GIA) since 12 cal. ka. Accounting for an anticipated uplift and tilting in this area reaching Assuming this area has been uplifted by a maximum of ~100 m (Ojala et al., 2013; Rosentau et al., 2021) is likely to increase the volume of melt delivered to the bed by elevating the mean annual

air temperature by up to would have been higher during the Younger Dryas due to higher temperatures ($\leq 0.75^{\circ}\text{C}$ where uplift rates are highest, which will) at lower altitude. Accounting for this would result in higher discharge channels that persist further upglacier of those high-uplift areas. Additional uncertainty arises from our estimated (and constant) meltwater and basal melt inputs, lack of diurnal forcing, fixed and spatially uniform basal velocity, fixed conductivity parameters (in both space and time), fixed semi-circular channel geometry, assumed water turbulence, pervasive hydraulic connectivity, lack of water flux from abutting ice, and randomly seeded moulin inputs. Initial sensitivity testing of basal velocity forced to change seasonally does indicate that changes in basal velocity throughout the year is important for repressurising the system each winter to more closely match borehole records (e.g., Doyle et al., 2018, 2022). Changes in geometry are also known to be important in synthetic experiments of GlaDS (see Hayden and Dow, 2023) whereas we kept ice geometry fixed here. Finally, we note that in its uncoupled configuration, GlaDS does not account for a reduction in the frictional resistance to ice flow where *overburden%* exceeds 100% or the increase in cavity closure rates that would accompany the increase in basal velocity associated with such a change in friction. In reality, sustained summer *overburden%* $\geq 100\%$ would result in the decoupling of the ice from the underlying bed as is suggested to be the reason for the limited observations of deformational structures within murto sediment exposures (e.g., Peterson Becher and Johnson, 2021; Mäkinen et al., 2023; Hovikoski et al., 2023). Future work should seek to address some of these limitations by including, for example, a more variable climate or coupled ice dynamics whereby the frictional resistance to ice flow is allowed to vary in response to changes *overburden%* (as in Ehrenfeucht et al., 2023). Initial sensitivity testing of basal velocity forced to change seasonally does indicate that changes in basal velocity throughout the year is important for repressurising the system each winter to more closely match borehole records (e.g., Doyle et al., 2018, 2022).

615 6 Summary and conclusions

In this paper we present the first application of a modern, process based subglacial hydrology model to the palaeo setting. We compared model outputs from the Glacier Drainage System model (GlaDS) against the predicted conditions associated with murto genesis. Murtoos are a unique glaciofluvial landform, identified throughout Finland and Sweden in terrain formerly occupied by the Fennoscandian Ice Sheet (FIS). The alternating sedimentological sequence of upper and lower flow regimes preserved within murtoos suggest that they formed amongst a network of small channels and cavities subject to rapid changes in water discharge and where water pressure met or exceeded ice overburden pressure. Further, their spatial distribution, rarely found closer than 40 km from the ice margin and often found downstream of ribbed moraines and upstream of eskers, suggests that murtoos represent the glaciofluvial imprint of a spatial and/or temporal transition between distributed and channelised drainage. We modelled this system using a setup representative of the Finnish Lake District Ice Lobe (FLDIL) at the end of the Younger Dryas, ~ 12 cal. ka. Our model was forced with a positive degree model representative of the palaeo climate, as well as a modified digital elevation model and reconstructed ice surface elevation representative of the same time period.

Our model outputs reproduce many of the conditions predicted for murto genesis including:

- i. An extensive area of water pressure at or equal to ice overburden pressure 40–60 km from the ice margin, largely robust to the range of parameters tested here.

630 ii. The annual evolution of a semi-distributed drainage system, which matches many of the anticipated conditions for murtoo
genesis.

635 iii. Modelled channels which extend 40–50 km from the ice margin ~~extending~~ upglacier into the hypothesised transitional
drainage zone associated with murtoo formation. These channels also have a similar spacing and geometry to mapped
eskers in the region.

640 iv. A statistically meaningful difference between areas of the bed without any indication of meltwater flow and areas of the
bed with meltwater routes or murtoo routes.

~~Murtoo fields are not universally present where the conditions for their formation are predicted in our model, particularly
within the centre of the FLDIL lobe, and we interpret this as a lack of upstream sediment supply further compounded by the
high-density of terrain-obseuring lakes in this area.~~ Additionally, we find a statistically meaningful difference in water pressure,
640 water velocity, and sheet/channel discharge, between meltwater routes and murtoo routes. We interpret this as a combination of
patchy murtoo distribution and ~~internal model dynamics relating to the radial geometry of the lobe~~^{the presence of overwinter}
~~channels in our model outputs.~~ Murtoo fields are not universally present where the conditions for their formation are predicted
645 in our model, particularly within the centre of the FLDIL lobe, this may arise from necessary simplifications in our modelling
which include the lack of sediment dynamics and/or coupling to ice flow. Nonetheless, many of our model outcomes from
650 the baseline model, in particular the area of high water pressure 40–60 km from the ice margin, are robust across the majority
of 29 sensitivity tests carried out here, in which various values for model parameters and boundary conditions were tested
within a range of numerical stability. At extremely high and low values of conductivity, parameters controlling how readily
water flows through the distributed or channelised system, water was evacuated from the system too easily or slowly to form
meaningful channels. Channels are also restricted when the highest moulin density was tested. However, across all other tests,
655 including random mesh geometries, alternate bed topographies, changing basal velocity, and changing moulin density, similar
patterns of modelled channels and water pressures emerge. Although our system is necessarily an idealised representation of
the study area—not including adjacent and abutting ice lobes, an upstream catchment area, or a coupled representation of
ice dynamics and basal hydrology—this work nonetheless demonstrates the potential application of modern process based
hydrology models to the palaeo setting, where model outputs can be directly compared to geomorphology and specific models
of landform genesis.

Code and data availability. All geophysical data used to parameterise the modelling (e.g., Quaternary sediment thickness, geothermal heat flux, lake bathymetry) is available from Finnish Geological Survey’s ‘Hakku’ service (<https://hakku GTK.fi/?locale=en>, last accessed on 06-09-2023). The Copernicus DEM used as basal elevation is available from: <https://spacedata.copernicus.eu/collections/copernicus-digital-elevation-model> (last accessed on 06-09-2023). For our modelling we used the Ice-sheet and Sea-level System Model (Larour et al., 2012)
660 revision 27448 available from: <https://issm.jpl.nasa.gov/> (last accessed on 06-09-2023). Murtoo field locations from Ahokangas et al.

(2021), glacial landforms shapefile data from Palmu et al. (2021), model results, and example input scripts used to produce and plot those results are available at the repository linked to this manuscript (<https://doi.org/10.5281/zenodo.8344208>, Hepburn et al., 2023)

Video supplement. Movie A1 is available at the online repository linked to this article (<https://doi.org/10.5281/zenodo.8344208>, Hepburn et al., 2023).

665 *Author contributions.* A.O, J.M, and C.F.D conceived the study, A.J.H designed and carried out the study and wrote the manuscript, all authors commented on the writing and helped with the analysis and interpretation.

Competing interests. The authors declare that no competing interests are present

670 *Acknowledgements.* This work forms part of the RewarD project (MUST consortium, University of Turku), funded by the Academy of Finland (grant numbers 322243/J.M and 322252/A.O). A.J.H is funded by a 150th Anniversary Vice Chancellor's Fellowship at Aberystwyth University, C.F.D is funded by the Canada Research Chair program (950-231237). All simulations were run on the Digital Research Alliance of Canada compute cluster, and we thank the European Union and the Finnish Geological Survey for enabling access to the data used to parameterise our model. We thank M. Werder for making the GlaDS model available, and we also thank M. Morlighem, J. Quinn, and J. Cuzzone for their help with ISSM. Finally, we thank L. Tarasov, S. Greenwood, and an anonymous reviewer for their suggestions to improve this paper.

Abatzoglou, J. T., Dobrowski, S. Z., Parks, S. A., and Hegewisch, K. C.: TerraClimate, a high-resolution global dataset of monthly climate and climatic water balance from 1958–2015, *Scientific data*, 5, 1–12, 2018.

Åhokangas, E., Ojala, A. E., Tuunainen, A., Valkama, M., Palmu, J.-P., Kajuutti, K., and Mäkinen, J.: The distribution of glacial meltwater routes and associated murtoo fields in Finland, *Geomorphology*, 389, 107 854, 2021.

Åkesson, H., Morlighem, M., Nisancioglu, K. H., Svendsen, J. I., and Mangerud, J.: Atmosphere-driven ice sheet mass loss paced by topography: Insights from modelling the south-western Scandinavian Ice Sheet, *Quaternary Science Reviews*, 195, 32–47, 2018.

Amon, L., Wagner-Cremer, F., Vassiljev, J., and Veski, S.: Spring onset and seasonality patterns during the Late Glacial period in the eastern Baltic region, *Climate of the Past*, 18, 2143–2153, 2022.

Andrews, L. C., Catania, G. A., Hoffman, M. J., Gulley, J. D., Lüthi, M. P., Ryser, C., Hawley, R. L., and Neumann, T. A.: Direct observations of evolving subglacial drainage beneath the Greenland Ice Sheet, *Nature*, 514, 80–83, 2014.

Archer, R., Ely, J. C., Heaton, T., Butcher, F. E., Hughes, A. L., and Clark, C. D.: Assessing ice sheet models against the landform record: The Likelihood of Accordant Lineations Analysis (LALA) tool, *Earth Surface Processes and Landforms*, 48, 2754–2771, 2023.

Banwell, A. F., Willis, I. C., and Arnold, N. S.: Modeling subglacial water routing at Paakitsoq, W Greenland, *Journal of Geophysical Research: Earth Surface*, 118, 1282–1295, 2013.

Beaud, F., Flowers, G. E., and Pimentel, S.: Seasonal-scale abrasion and quarrying patterns from a two-dimensional ice-flow model coupled to distributed and channelized subglacial drainage, *Geomorphology*, 219, 176–191, 2014.

Beaud, F., Flowers, G. E., and Venditti, J. G.: Modeling sediment transport in ice-walled subglacial channels and its implications for esker formation and proglacial sediment yields, *Journal of Geophysical Research: Earth Surface*, 123, 3206–3227, 2018.

Bingham, R. G., King, E. C., Smith, A. M., and Pritchard, H. D.: Glacial geomorphology: towards a convergence of glaciology and geomorphology, *Progress in Physical Geography*, 34, 327–355, 2010.

Boswell, S. M., Toucanne, S., Pitel-Roudaut, M., Creyts, T. T., Eynaud, F., and Bayon, G.: Enhanced surface melting of the Fennoscandian Ice Sheet during periods of North Atlantic cooling, *Geology*, 47, 664–668, 2019.

Boulton, G. and Haggdorn, M.: Glaciology of the British Isles Ice Sheet during the last glacial cycle: form, flow, streams and lobes, *Quaternary Science Reviews*, 25, 3359–3390, 2006.

Boulton, G. and Jones, A.: Stability of temperate ice caps and ice sheets resting on beds of deformable sediment, *Journal of Glaciology*, 24, 29–43, 1979.

Boulton, G., Lunn, R., Vidstrand, P., and Zatsepin, S.: Subglacial drainage by groundwater-channel coupling, and the origin of esker systems: part I glaciological observations, *Quaternary Science Reviews*, 26, 1067–1090, 2007a.

Boulton, G., Lunn, R., Vidstrand, P., and Zatsepin, S.: Subglacial drainage by groundwater–channel coupling, and the origin of esker systems: part II theory and simulation of a modern system, *Quaternary Science Reviews*, 26, 1091–1105, 2007b.

Boulton, G., Haggdorn, M., Maillot, P., and Zatsepin, S.: Drainage beneath ice sheets: groundwater–channel coupling, and the origin of esker systems from former ice sheets, *Quaternary Science Reviews*, 28, 621–638, 2009.

Bradwell, T.: Identifying palaeo-ice-stream tributaries on hard beds: Mapping glacial bedforms and erosion zones in NW Scotland, *Geomorphology*, 201, 397–414, 2013.

710 Braithwaite, R. J. and Olesen, O. B.: Calculation of glacier ablation from air temperature, West Greenland, in: *Glacier Fluctuations and Climatic Change: Proceedings of the Symposium on Glacier Fluctuations and Climatic Change*, held in Amsterdam, 1–5 June 1987, pp. 219–233, Springer, 1989.

Budd, W., Keage, P., and Blundy, N.: Empirical studies of ice sliding, *Journal of glaciology*, 23, 157–170, 1979.

Chandler, D., Wadham, J., Lis, G., Cowton, T., Sole, A., Bartholomew, I., Telling, J., Nienow, P., Bagshaw, E., Mair, D., et al.: Evolution of 715 the subglacial drainage system beneath the Greenland Ice Sheet revealed by tracers, *Nature Geoscience*, 6, 195–198, 2013.

Chandler, D. M., Wadham, J. L., Nienow, P. W., Doyle, S. H., Tedstone, A. J., Telling, J., Hawkings, J., Alcock, J. D., Linhoff, B., and Hubbard, A.: Rapid development and persistence of efficient subglacial drainage under 900 m-thick ice in Greenland, *Earth and Planetary Science Letters*, 566, 116 982, 2021.

Chu, V. W.: Greenland ice sheet hydrology: A review, *Progress in Physical Geography*, 38, 19–54, 2014.

720 Clark, P. U. and Walder, J. S.: Subglacial drainage, eskers, and deforming beds beneath the Laurentide and Eurasian ice sheets, *Geological Society of America Bulletin*, 106, 304–314, 1994.

Cofaigh, C. Ó.: Tunnel valley genesis, *Progress in physical geography*, 20, 1–19, 1996.

Cook, S. J., Christoffersen, P., Todd, J., Slater, D., and Chauché, N.: Coupled modelling of subglacial hydrology and calving-front melting 725 at Store Glacier, West Greenland, *The Cryosphere*, 14, 905–924, 2020.

Cook, S. J., Christoffersen, P., and Todd, J.: A fully-coupled 3D model of a large Greenlandic outlet glacier with evolving subglacial hydrology, frontal plume melting and calving, *Journal of Glaciology*, 68, 486–502, 2022.

Coughlan, M., Tóth, Z., Van Landeghem, K. J., Mccarron, S., and Wheeler, A. J.: Formational history of the Wicklow Trough: a marine-transgressed tunnel valley revealing ice flow velocity and retreat rates for the largest ice stream draining the late-Devensian British–Irish 730 Ice Sheet, *Journal of Quaternary Science*, 35, 907–919, 2020.

Cuffey, K. M. and Paterson, W. S. B.: *The physics of glaciers*, Academic Press, 2010.

Cuzzone, J. K., Schlegel, N.-J., Morlighem, M., Larour, E., Briner, J. P., Seroussi, H., and Caron, L.: The impact of model resolution on 735 the simulated Holocene retreat of the southwestern Greenland ice sheet using the Ice Sheet System Model (ISSM), *The Cryosphere*, 13, 879–893, 2019.

Davison, B. J., Sole, A. J., Livingstone, S. J., Cowton, T. R., and Nienow, P. W.: The influence of hydrology on the dynamics of land- 740 terminating sectors of the Greenland ice sheet, *Frontiers in Earth Science*, 7, 10, 2019.

De Fleurian, B., Morlighem, M., Seroussi, H., Rignot, E., van den Broeke, M. R., Kuipers Munneke, P., Mouginot, J., Smeets, P. C., and Tedstone, A. J.: A modeling study of the effect of runoff variability on the effective pressure beneath Russell Glacier, West Greenland, *Journal of Geophysical Research: Earth Surface*, 121, 1834–1848, 2016.

Dewald, N., Lewington, E. L., Livingstone, S. J., Clark, C. D., and Storrar, R. D.: Distribution, characteristics and formation of esker 745 enlargements, *Geomorphology*, 392, 107 919, 2021.

Dewald, N., Livingstone, S. J., and Clark, C. D.: Subglacial meltwater routes of the Fennoscandian Ice Sheet, *Journal of Maps*, 18, 382–396, 2022.

Donner, J.: The Younger Dryas age of the Salpausselkä moraines in Finland, *Bulletin of the Geological Society of Finland*, 82, 69–80, 2010.

Dow, C., Werder, M., Nowicki, S., and Walker, R.: Modeling Antarctic subglacial lake filling and drainage cycles., *Cryosphere Discussions*, 750 9, 2015.

Dow, C., McCormack, F., Young, D., Greenbaum, J., Roberts, J., and Blankenship, D.: Totten Glacier subglacial hydrology determined from geophysics and modeling, *Earth and Planetary Science Letters*, 531, 115 961, 2020.

Dow, C., Ross, N., Jeofry, H., Siu, K., and Siegert, M.: Antarctic basal environment shaped by high-pressure flow through a subglacial river system, *Nature Geoscience*, 15, 892–898, 2022.

750 Dow, C. F.: The role of subglacial hydrology in Antarctic ice sheet dynamics and stability: a modelling perspective, *Annals of Glaciology*, pp. 1–6, 2023.

Dow, C. F., Karlsson, N. B., and Werder, M. A.: Limited impact of subglacial supercooling freeze-on for Greenland ice sheet stratigraphy, *Geophysical Research Letters*, 45, 1481–1489, 2018a.

Dow, C. F., Lee, W. S., Greenbaum, J. S., Greene, C. A., Blankenship, D. D., Poinar, K., Forrest, A. L., Young, D. A., and Zappa, C. J.: Basal 755 channels drive active surface hydrology and transverse ice shelf fracture, *Science Advances*, 4, eaao7212, 2018b.

Dow, C. F., Werder, M., Babonis, G., Nowicki, S., Walker, R. T., Csathó, B., and Morlighem, M.: Dynamics of active subglacial lakes in Recovery Ice Stream, *Journal of Geophysical Research: Earth Surface*, 123, 837–850, 2018c.

Doyle, S. H., Hubbard, B., Christoffersen, P., Young, T. J., Hofstede, C., Bougamont, M., Box, J., and Hubbard, A.: Physical conditions of fast glacier flow: 1. Measurements from boreholes drilled to the bed of Store Glacier, West Greenland, *Journal of Geophysical Research: 760 Earth Surface*, 123, 324–348, 2018.

Doyle, S. H., Hubbard, B., Christoffersen, P., Law, R., Hewitt, D. R., Neufeld, J. A., Schoonman, C. M., Chudley, T. R., and Bougamont, M.: Water flow through sediments and at the ice-sediment interface beneath Sermeq Kujalleq (Store Glacier), Greenland, *Journal of Glaciology*, 68, 665–684, 2022.

Ehrenfeucht, S., Morlighem, M., Rignot, E., Dow, C. F., and Mouginot, J.: Seasonal acceleration of Petermann Glacier, Greenland, from 765 changes in subglacial hydrology, *Geophysical Research Letters*, 50, e2022GL098 009, 2023.

Fausto, R. S., Ahlstrøm, A. P., Van As, D., and Steffen, K.: Present-day temperature standard deviation parameterization for Greenland, *Journal of Glaciology*, 57, 1181–1183, 2011.

Felden, A. M., Martin, D. F., and Ng, E. G.: SUHMO: an adaptive mesh refinement SUbglacial Hydrology MOdel v1. 0, *Geoscientific Model 770 Development*, 16, 407–425, 2023.

Flowers, G. E.: Hydrology and the future of the Greenland Ice Sheet, *Nature communications*, 9, 2729, 2018.

Gandy, N., Gregoire, L. J., Ely, J. C., Cornford, S. L., Clark, C. D., and Hodgson, D. M.: Exploring the ingredients required to successfully 775 model the placement, generation, and evolution of ice streams in the British-Irish Ice Sheet, *Quaternary Science Reviews*, 223, 105 915, 2019.

Gandy, N., Gregoire, L. J., Ely, J. C., Cornford, S. L., Clark, C. D., and Hodgson, D. M.: Collapse of the last Eurasian Ice Sheet in the North 780 Sea modulated by combined processes of ice flow, surface melt, and marine ice sheet instabilities, *Journal of Geophysical Research: Earth Surface*, 126, e2020JF005 755, 2021.

García-Ruiz, J. M., Hughes, P. D., Palacios, D., and Andrés, N.: The European glacial landscapes from the main deglaciation, in: *European Glacial Landscapes*, pp. 243–259, Elsevier, 2023.

Gardner, A. S., Sharp, M. J., Koerner, R. M., Labine, C., Boon, S., Marshall, S. J., Burgess, D. O., and Lewis, D.: Near-surface temperature 785 lapse rates over Arctic glaciers and their implications for temperature downscaling, *Journal of Climate*, 22, 4281–4298, 2009.

Greenwood, S. L., Clason, C. C., Helanow, C., and Margold, M.: Theoretical, contemporary observational and palaeo-perspectives on ice sheet hydrology: processes and products, *Earth-Science Reviews*, 155, 1–27, 2016.

Greenwood, S. L., Clason, C. C., Nyberg, J., Jakobsson, M., and Holmlund, P.: The Bothnian Sea ice stream: early Holocene retreat dynamics of the south-central Fennoscandian Ice Sheet, *Boreas*, 46, 346–362, 2017.

785 GTK, Finland: Superficial deposits of Finland 1:200 000 (sediment polygons), https://tupa GTK.fi/paikkatieto/meta/maapera_200k.html#tun_nistamistiedo, 2010.

Harper, J., Meierbacholt, T., Humphrey, N., Saito, J., and Stansberry, A.: Generation and fate of basal meltwater during winter, western Greenland Ice Sheet, *The Cryosphere*, 15, 5409–5421, 2021.

790 Hayden, A.-M. and Dow, C. F.: Examining the effect of ice dynamic changes on subglacial hydrology through modelling of a synthetic Antarctic glacier, *Journal of Glaciology*, pp. 1–14, 2023.

Hepburn, A., Dow, C., Ojala, A., Mäkinen, J., Ahokangas, E., Hovikoski, J., Jukka-Pekka, P., and Kajuutti, K.: Supplementary material for 'Reorganisation of subglacial drainage processes during rapid melting of the Fennoscandian Ice Sheet', <https://doi.org/10.5281/zenodo.8344208>, 2023.

Hewitt, I. J.: Modelling distributed and channelized subglacial drainage: the spacing of channels, *Journal of Glaciology*, 57, 302–314, 2011.

795 Hewitt, I. J. and Creyts, T. T.: A model for the formation of eskers, *Geophysical Research Letters*, 46, 6673–6680, 2019.

Hill, T., Flowers, G. E., Hoffman, M. J., Bingham, D., and Werder, M. A.: Improved representation of laminar and turbulent sheet flow in subglacial drainage models, *Journal of Glaciology*, pp. 1–14, 2023.

Hoffman, M. J., Andrews, L. C., Price, S. F., Catania, G. A., Neumann, T. A., Lüthi, M. P., Gulley, J., Ryser, C., Hawley, R. L., and Morriss, B.: Greenland subglacial drainage evolution regulated by weakly connected regions of the bed, *Nature communications*, 7, 13 903, 2016.

800 Hooke, R. L.: Englacial and subglacial hydrology: a qualitative review, *Arctic and Alpine Research*, 21, 221–233, 1989.

Hovikoski, J., Mäkinen, J., Winsemann, J., Soini, S., Kajuutti, K., Hepburn, A., and Ojala, A.: Upper-flow regime bedforms in a subglacial triangular-shaped landform (murtoo), late Pleistocene, SW Finland: Implications for flow dynamics and sediment transport in (semi-) distributed subglacial meltwater drainage systems, *Sedimentary Geology*, p. 106448, 2023.

Hughes, A. L., Gyllencreutz, R., Lohne, Ø. S., Mangerud, J., and Svendsen, J. I.: The last Eurasian ice sheets—a chronological database and 805 time-slice reconstruction, *DATED-1*, *Boreas*, 45, 1–45, 2016.

Indigo, C., Dow, C. F., Greenbaum, J. S., and Morlighem, M.: Drygalski Ice Tongue stability influenced by rift formation and ice morphology, *Journal of Glaciology*, 67, 243–252, 2021.

Johnsen, S. J., Clausen, H. B., Dansgaard, W., Gundestrup, N. S., Hammer, C. U., Andersen, U., Andersen, K. K., Hvidberg, C. S., Dahl-Jensen, D., Steffensen, J. P., et al.: The $\delta^{18}\text{O}$ record along the Greenland Ice Core Project deep ice core and the problem of possible 810 Eemian climatic instability, *Journal of Geophysical Research: Oceans*, 102, 26 397–26 410, 1997.

Kamb, B.: Glacier surge mechanism based on linked cavity configuration of the basal water conduit system, *Journal of Geophysical Research: Solid Earth*, 92, 9083–9100, 1987.

Karlsson, N. B. and Dahl-Jensen, D.: Response of the large-scale subglacial drainage system of Northeast Greenland to surface elevation changes, *The Cryosphere*, 9, 1465–1479, 2015.

815 Karlsson, N. B., Solgaard, A. M., Mankoff, K. D., Gillet-Chaulet, F., MacGregor, J. A., Box, J. E., Citterio, M., Colgan, W. T., Larsen, S. H., Kjeldsen, K. K., et al.: A first constraint on basal melt-water production of the Greenland ice sheet, *Nature Communications*, 12, 3461, 2021.

Kazmierczak, E., Sun, S., Coulon, V., and Pattyn, F.: Subglacial hydrology modulates basal sliding response of the Antarctic ice sheet to climate forcing, *The Cryosphere*, 16, 4537–4552, 2022.

820 Kirkham, J. D., Hogan, K. A., Larter, R. D., Arnold, N. S., Ely, J. C., Clark, C. D., Self, E., Games, K., Huuse, M., Stewart, M. A., et al.: Tunnel valley formation beneath deglaciating mid-latitude ice sheets: Observations and modelling, *Quaternary Science Reviews*, p. 107680, 2022.

Kirkham, J. D., Hogan, K. A., Larter, R. D., Self, E., Games, K., Huuse, M., Stewart, M. A., Ottesen, D., Le Heron, D. P., Lawrence, A., et al.: The infill of tunnel valleys in the central North Sea: Implications for sedimentary processes, geohazards, and ice-sheet dynamics, 825 *Marine Geology*, 467, 107 185, 2024.

Kleman, J., Hättestrand, C., Borgström, I., and Stroeve, A.: Fennoscandian palaeoglaciology reconstructed using a glacial geological inversion model, *Journal of glaciology*, 43, 283–299, 1997.

Kleman, J., Hättestrand, C., Stroeve, A. P., Jansson, K. N., De Angelis, H., and Borgström, I.: Reconstruction of Palaeo-Ice Sheets-Inversion of their Glacial Geomorphological Record, *Glacier science and environmental change*, pp. 192–198, 2006.

830 Larour, E., Seroussi, H., Morlighem, M., and Rignot, E.: Continental scale, high order, high spatial resolution, ice sheet modeling using the Ice Sheet System Model (ISSM), *Journal of Geophysical Research: Earth Surface*, 117, 2012.

Lehtinen, M., Nurmi, P. A., and Ramo, O.: *Precambrian Geology of Finland*, Elsevier, 2005.

Lewington, E. L., Livingstone, S. J., Clark, C. D., Sole, A. J., and Storrar, R. D.: A model for interaction between conduits and surrounding hydraulically connected distributed drainage based on geomorphological evidence from Keewatin, Canada, *The Cryosphere*, 14, 2949–2976, 835 2020.

Livingstone, S., Clark, C., Woodward, J., and Kingslake, J.: Potential subglacial lakes and meltwater drainage pathways beneath the Antarctic and Greenland ice sheets, *The Cryosphere*, 7, 1721–1740, 2013a.

Livingstone, S. J., Clark, C. D., and Tarasov, L.: Modelling North American palaeo-subglacial lakes and their meltwater drainage pathways, *Earth and Planetary Science Letters*, 375, 13–33, 2013b.

840 Livingstone, S. J., Storrar, R. D., Hillier, J. K., Stokes, C. R., Clark, C. D., and Tarasov, L.: An ice-sheet scale comparison of eskers with modelled subglacial drainage routes, *Geomorphology*, 246, 104–112, 2015.

Lunkka, J. P. and Erikkilä, A.: Behaviour of the lake district ice lobe of the Scandinavian ice sheet during the younger dryas chronozone (ca. 12 800–11 500 years ago), *Tech. rep.*, Posiva Oy, 2012.

Lunkka, J. P., Palmu, J.-P., and Seppänen, A.: Deglaciation dynamics of the Scandinavian Ice Sheet in the Salpausselkä zone, southern 845 Finland, *Boreas*, 50, 404–418, 2021.

MacAyeal, D. R.: Large-scale ice flow over a viscous basal sediment: Theory and application to ice stream B, Antarctica, *Journal of Geophysical Research: Solid Earth*, 94, 4071–4087, 1989.

Mäkinen, J.: Time-transgressive deposits of repeated depositional sequences within interlobate glaciofluvial (esker) sediments in Köyliö, SW Finland, *Sedimentology*, 50, 327–360, 2003.

850 Mäkinen, J., Kajuutti, K., Palmu, J.-P., Ojala, A., and Ahokangas, E.: Triangular-shaped landforms reveal subglacial drainage routes in SW Finland, *Quaternary Science Reviews*, 164, 37–53, 2017.

Mäkinen, J., Kajuutti, K., Ojala, A. E., Ahokangas, E., Tuunainen, A., Valkama, M., and Palmu, J.-P.: Genesis of subglacial triangular-shaped landforms (murtoos) formed by the Fennoscandian Ice Sheet, *Earth Surface Processes and Landforms*, 2023.

Mangerud, J., Hughes, A. L., Johnson, M. D., and Lunkka, J. P.: The Fennoscandian Ice Sheet during the Younger Dryas Stadial, in: *European 855 Glacial landscapes*, pp. 437–452, Elsevier, 2023.

Marshall, S. J. and Sharp, M. J.: Temperature and melt modeling on the Prince of Wales ice field, Canadian High Arctic, *Journal of Climate*, 22, 1454–1468, 2009.

McArthur, K., McCormack, F. S., and Dow, C. F.: Basal conditions of Denman Glacier from glacier hydrology and ice dynamics modeling, *The Cryosphere Discussions*, pp. 1–29, 2023.

860 Nick, F. M., Vieli, A., Andersen, M. L., Joughin, I., Payne, A., Edwards, T. L., Pattyn, F., and van de Wal, R. S.: Future sea-level rise from
Greenlands main outlet glaciers in a warming climate, *Nature*, 497, 235–238, 2013.

Nienow, P., Sole, A., Slater, D. A., and Cowton, T.: Recent advances in our understanding of the role of meltwater in the Greenland Ice Sheet
system, *Current Climate Change Reports*, 3, 330–344, 2017.

Nye, J.: Water at the bed of a glacier, in: International Glaciological Society, pp. 189–194, 1972.

865 Ojala, A. E., Palmu, J.-P., Åberg, A., Åberg, S., and Virkki, H.: Development of an ancient shoreline database to reconstruct the Litorina Sea
maximum extension and the highest shoreline of the Baltic Sea basin in Finland, *Bulletin of the Geological Society of Finland*, 2013.

Ojala, A. E., Peterson Becher, G., Mäkinen, J., Johnson, M. D., Kajuutti, K., Palmu, J.-P., Ahokangas, E., and Öhrling, C.: Ice-sheet scale
distribution and morphometry of triangular-shaped hummocks (murtoos): a subglacial landform produced during rapid retreat of the
Scandinavian Ice Sheet, *Annals of Glaciology*, 60, 115–126, 2019.

870 Ojala, A. E., Mäkinen, J., Ahokangas, E., Kajuutti, K., Valkama, M., Tuunainen, A., and Palmu, J.-P.: Diversity of murtoos and murtoo-related
subglacial landforms in the Finnish area of the Fennoscandian Ice Sheet, *Boreas*, 50, 1095–1115, 2021.

Ojala, A. E., Mäkinen, J., Kajuutti, K., Ahokangas, E., and Palmu, J.-P.: Subglacial evolution from distributed to channelized drainage:
evidence from the Lake Murtoo area in SW Finland, *Earth Surface Processes and Landforms*, 47, 2877–2896, 2022.

Palmu, J.-P., Ojala, A. E., Virtasalo, J., Putkinen, N., Kohonen, J., and Sarala, P.: Classification system of superficial (quaternary) geological
875 units in Finland, *Developments in Map Data Management and Geological Unit Nomenclature in Finland*, 412, 115–169, 2021.

Patton, H., Hubbard, A., Andreassen, K., Auriac, A., Whitehouse, P. L., Stroeve, A. P., Shackleton, C., Winsborrow, M., Heyman, J., and
Hall, A. M.: Deglaciation of the Eurasian ice sheet complex, *Quaternary Science Reviews*, 169, 148–172, 2017.

Peterson, G., Johnson, M. D., and Smith, C. A.: Glacial geomorphology of the south Swedish uplands—focus on the spatial distribution of
hummock tracts, *Journal of Maps*, 13, 534–544, 2017.

880 Peterson Becher, G. and Johnson, M. D.: Sedimentology and internal structure of murtoos-V-shaped landforms indicative of a dynamic
subglacial hydrological system, *Geomorphology*, 380, 107 644, 2021.

Poinar, K., Dow, C. F., and Andrews, L. C.: Long-term support of an active subglacial hydrologic system in Southeast Greenland by firn
aquifers, *Geophysical Research Letters*, 46, 4772–4781, 2019.

Putkinen, N., Eyles, N., Putkinen, S., Ojala, A. E., Palmu, J.-P., Sarala, P., Väänänen, T., Räisänen, J., Saarelainen, J., Ahtonen, N., et al.:
885 High-resolution LiDAR mapping of glacial landforms and ice stream lobes in Finland., *Bulletin of the Geological Society of Finland*, 89,
2017.

Rada, C. and Schoof, C.: Channelized, distributed, and disconnected: subglacial drainage under a valley glacier in the Yukon, *The Cryosphere*,
12, 2609–2636, 2018.

Rada Giacaman, C. A. and Schoof, C.: Channelized, distributed, and disconnected: spatial structure and temporal evolution of the subglacial
890 drainage under a valley glacier in the Yukon, *The Cryosphere*, 17, 761–787, 2023.

Rampton, V.: Large-scale effects of subglacial meltwater flow in the southern Slave Province, Northwest Territories, Canada, *Canadian
Journal of Earth Sciences*, 37, 81–93, 2000.

Regnél, C., Mangerud, J., and Svendsen, J. I.: Tracing the last remnants of the Scandinavian Ice Sheet: Ice-dammed lakes and a catastrophic
outburst flood in northern Sweden, *Quaternary Science Reviews*, 221, 105 862, 2019.

895 Rosentau, A., Klemann, V., Bennike, O., Steffen, H., Wehr, J., Latinović, M., Bagge, M., Ojala, A., Berglund, M., Peterson Becher, G., et al.:
A Holocene relative sea-level database for the Baltic Sea, *Quaternary Science Reviews*, 266, 107 071, 2021.

Röthlisberger, H.: Water pressure in intra-and subglacial channels, *Journal of Glaciology*, 11, 177–203, 1972.

Schenk, F., Välimäki, M., Muschitiello, F., Tarasov, L., Heikkilä, M., Björck, S., Brandefelt, J., Johansson, A. V., Näslund, J.-O., and Wohlfarth, B.: Warm summers during the Younger Dryas cold reversal, *Nature Communications*, 9, 1634, 2018.

900 Scholzen, C., Schuler, T. V., and Gilbert, A.: Sensitivity of subglacial drainage to water supply distribution at the Kongsfjord basin, Svalbard, *The Cryosphere*, 15, 2719–2738, 2021.

Schoof, C.: Ice-sheet acceleration driven by melt supply variability, *Nature*, 468, 803–806, 2010.

Shackleton, C., Patton, H., Hubbard, A., Winsborrow, M., Kingslake, J., Esteves, M., Andreassen, K., and Greenwood, S. L.: Subglacial water storage and drainage beneath the Fennoscandian and Barents Sea ice sheets, *Quaternary Science Reviews*, 201, 13–28, 2018.

905 Sole, A., Nienow, P., Bartholomew, I., Mair, D., Cowton, T., Tedstone, A., and King, M. A.: Winter motion mediates dynamic response of the Greenland Ice Sheet to warmer summers, *Geophysical Research Letters*, 40, 3940–3944, 2013.

Sommers, A., Meyer, C., Morlighem, M., Rajaram, H., Poinar, K., Chu, W., and Mejia, J.: Subglacial hydrology modeling predicts high winter water pressure and spatially variable transmissivity at Helheim Glacier, Greenland, *Journal of Glaciology*, pp. 1–13, 2022.

910 Stokes, C. R., Tarasov, L., Blomdin, R., Cronin, T. M., Fisher, T. G., Gyllencreutz, R., Hättestrand, C., Heyman, J., Hindmarsh, R. C., Hughes, A. L., et al.: On the reconstruction of palaeo-ice sheets: Recent advances and future challenges, *Quaternary Science Reviews*, 125, 15–49, 2015.

Storrar, R. D. and Livingstone, S. J.: Glacial geomorphology of the northern Kivalliq region, Nunavut, Canada, with an emphasis on meltwater drainage systems, *Journal of Maps*, 13, 153–164, 2017.

915 Stroeven, A. P., Hättestrand, C., Kleman, J., Heyman, J., Fabel, D., Fredin, O., Goodfellow, B. W., Harbor, J. M., Jansen, J. D., Olsen, L., et al.: Deglaciation of fennoscandia, *Quaternary Science Reviews*, 147, 91–121, 2016.

Tarasov, L., Dyke, A. S., Neal, R. M., and Peltier, W. R.: A data-calibrated distribution of deglacial chronologies for the North American ice complex from glaciological modeling, *Earth and Planetary Science Letters*, 315, 30–40, 2012.

Tedstone, A. J., Nienow, P. W., Gourmelen, N., Dehecq, A., Goldberg, D., and Hanna, E.: Decadal slowdown of a land-terminating sector of the Greenland Ice Sheet despite warming, *Nature*, 526, 692–695, 2015.

920 Utting, D. J., Ward, B. C., and Little, E. C.: Genesis of hummocks in glaciofluvial corridors near the Keewatin Ice Divide, Canada, *Boreas*, 38, 471–481, 2009.

Van Boeckel, M., Van Boeckel, T., and Hall, A. M.: Late erosion pulse triggered by rapid melt in the cold-based interior of the last Fennoscandian Ice Sheet, an example from Rogen, *Earth Surface Processes and Landforms*, 47, 3376–3394, 2022.

925 Van de Wal, R., Smeets, C., Boot, W., Stoffelen, M., Van Kampen, R., Doyle, S. H., Wilhelms, F., van den Broeke, M. R., Reijmer, C., Oerlemans, J., et al.: Self-regulation of ice flow varies across the ablation area in south-west Greenland, *The Cryosphere*, 9, 603–611, 2015.

van den Broeke, M., Bus, C., Ettema, J., and Smeets, P.: Temperature thresholds for degree-day modelling of Greenland ice sheet melt rates, *Geophysical Research Letters*, 37, 2010.

930 van den Broeke, M. R., Kuipers Munneke, P., Noël, B., Reijmer, C., Smeets, P., van de Berg, W. J., and van Wessem, J. M.: Contrasting current and future surface melt rates on the ice sheets of Greenland and Antarctica: Lessons from in situ observations and climate models, *PLOS Climate*, 2, e00000 203, 2023.

Vérité, J., Ravier, É., Bourgeois, O., Bessin, P., Livingstone, S. J., Clark, C. D., Pochat, S., and Mourguet, R.: Formation of murtoos by repeated flooding of ribbed bedforms along subglacial meltwater corridors, *Geomorphology*, 408, 108 248, 2022.

935 Wake, L. and Marshall, S.: Assessment of current methods of positive degree-day calculation using in situ observations from glaciated regions, *Journal of Glaciology*, 61, 329–344, 2015.

Walder, J. S.: Hydraulics of subglacial cavities, *Journal of Glaciology*, 32, 439–445, 1986.

Weertman, J.: General theory of water flow at the base of a glacier or ice sheet, *Reviews of Geophysics*, 10, 287–333, 1972.

Werder, M. A., Hewitt, I. J., Schoof, C. G., and Flowers, G. E.: Modeling channelized and distributed subglacial drainage in two dimensions, *Journal of Geophysical Research: Earth Surface*, 118, 2140–2158, 2013.

940 Wright, P. J., Harper, J. T., Humphrey, N. F., and Meierbachtol, T. W.: Measured basal water pressure variability of the western Greenland Ice Sheet: Implications for hydraulic potential, *Journal of Geophysical Research: Earth Surface*, 121, 1134–1147, 2016.

Yang, K. and Smith, L. C.: Internally drained catchments dominate supraglacial hydrology of the southwest Greenland Ice Sheet, *Journal of Geophysical Research: Earth Surface*, 121, 1891–1910, 2016.

Appendix: Contents

945 This file contains supplementary information for ‘*Reorganisation The organisation of subglacial drainage processes during rapid melting the demise of the Fennoscandian Ice SheetFinnish Lake District Ice-Lobe*’

Appendix A. Additional model description for the Glacier Drainage System model (GlaDS Werder et al., 2013).

Table A1. List of input values for GlaDS, values highlighted in bold indicate those used for sensitivity testing and a range of values is provided. Note, in all instances *sheet* refers to the subglacial drainage system.

950 **Movie A1.** Evolution of the system with respect to *overburden%* through time in the baseline model run. Model years 15–17 were arbitrarily chosen to illustrate the transient state of the system through several melt season cycles. Channels are shown as black lines where Q_c exceeds $1 \text{ m}^3 \text{ s}^{-1}$.

955 **Figure A1.** The distribution of meltwater routes, murtoo routes, and sediment in the Finnish Lake District Ice Lobe. **A)** Meltwater routes and murtoo routes as mapped by Ahokangas et al. (2021). There is a general absence of murtoos in the centre of the lobe 40–60 km from the ice margin. **B)** Sediment cover (GTK, Finland, 2010) showing thin sediment thickness in the terrain from which murtoos appear absent.

960 **Figure A2** Overwinter channels and their influence on subsequent summer drainage. **A)** Modelled channels in January, model year 15 in the baseline run (black lines). Channels are present overwinter in the outer two thirds of the FLDIL. **B)** Modelled channels in June, model year 15, near to the start of the melt season. Note that channels in the outer two thirds are already well established compared to those in the central third of the FLDIL. **C)** Modelled channels in January, model year 2016. Note that winter channels are now visible in the central third of the FLDIL. In all panels, background panels shows water pressure as a percentage of ice overburden pressure. Murtoo fields are shown as inverted black triangles. Each channel is defined where the median channel discharge, Q_c , exceeds $1 \text{ m}^3 \text{ s}^{-1}$.

965 **Figure A3.** Median *overburden%*, channel discharge, Q_c , and sheet discharge, q_s per timestep over the full length of the baseline model run.

970 **Figure A4–A32.** Comparison of the median summer system for the range of sensitivity parameters against the baseline model run. **A)** Water pressure expressed as a percentage of overburden pressure, *overburden%*. Channels are shown as black lines where median discharge exceeds $1 \text{ m}^3 \text{ s}^{-1}$. **B)** Baseline median summer *overburden%* minus the tested median summer *overburden%*. The same figure caption applies for Figures A4–A32.

975 **Figure A33.** Boxplots of model parameters grouped by month for overburden (*overburden%*, **A**), sheet discharge (q_s , **B**), water velocity (V_W , **C**), and channel discharge (Q_c , **D**) during all model years at nodes between 40–60 km from the ice margin. As in Figure 5, nodes that fall within meltwater routes which do host murtoos (murtoo routes) are shown in blue, nodes which fall within mapped meltwater routes that do not contain murtoo fields (meltwater routes) are shown in orange, and all other nodes are shown in purple. Medians for each group are shown as black circles, and ‘outliers’—defined as points more than 150% of the interquartile range away from the upper and lower quartile—are shown as crosses.

Tables A2–A5. Tukey-Kramer HSD test results for $overburden\%$ (Table A2), q_s (Table A3), Q_c (Table A4), and V_w (Table A5) in meltwater routes, murtoo routes, and non-meltwater routes between 40–60 km from the ice margin. The upper and lower limits describe the 95% confidence intervals for the true mean difference, A-B is the difference between group means.

Appendix A: Additional model description

980 In GlaDS (Werder et al., 2013) water flux, q_s , through the distributed system is driven by the hydraulic potential gradient, $\nabla\phi$, along with the sheet conductivity, k_s

$$q_s = -k_s h^\alpha |\nabla\phi|^\beta \nabla\phi, \quad (A1)$$

where the flow exponents, $\alpha = 5/4$ and $\beta = 3/2$ describe fully turbulent flow in the Darcy-Weishbach law, and h is the sheet thickness. The sheet thickness evolves through time given by

$$985 \quad \frac{\delta h}{\delta t} = w - v, \quad (A2)$$

for functions w and v which describe the cavity opening and closing rate respectively (Walder, 1986; Kamb, 1987). Basal sliding opens cavities at a rate given by the basal sliding speed, U_b acting over basal bumps with a height, h_r through

$$w(h) = \begin{cases} U_b (h_r - h) / l_r & \text{if } h < h_r \\ 0 & \text{otherwise} \end{cases} \quad (A3)$$

where l_r is the typical horizontal cavity spacing. In turn, viscous ice deformation leads to cavity closure, which is related to the 990 effective pressure, N by

$$v(h, N) = Ah|N|^{n-1}N, \quad (A4)$$

where A is the rate factor, or the rheological constant of ice, multiplied by a first order geometrical factor, and n is the Glen's flow law exponent. Sheet elements exchange water with channels and the cross sectional area of these channels S , evolves through time due to the dissipation of potential energy, Π , sensible heat exchange, Ξ , and cavity closure rates due to viscous 995 ice creep v_c

$$\frac{\partial S}{\partial t} = \frac{\Xi - \Pi}{\rho_i L} - v_c, \quad (A5)$$

where ρ_i is the ice density and L is the latent heat of fusion. The default parameters used here, as well as those sensitivity tested, are listed in Table A1.

Table A1. List of input values for GlaDS, values highlighted in bold indicate those used for sensitivity testing and a range of values is provided. Note, in all instances *sheet* refers to the subglacial drainage system.

Symbol	Description	Default value	Tested range	Units
ρ_i	ice density	918		kg m^{-3}
ρ_w	water density	1000		kg m^{-3}
g	gravitational acceleration	9.81		m s^{-2}
n	Glen's flow law exponent	3		
a	basal friction coefficient	0–120		$(\text{Pa a}^{-1})^{1/2}$
A	rate factor	1.7×10^{-24}		$\text{s}^{-1} \text{Pa}^{-3}$
L	latent heat	3.34×10^5		J kg^{-1}
c_t	pressure melt coefficient	7.5×10^{-8}		KPa^{-1}
c_w	heat capacity of water	4.22×10^3		$\text{J kg}^{-1} \text{K}^{-1}$
α	first sheet flow exponent	5/4		
β	second sheet flow exponent	3/2		
α_c	first channel flow exponent	5/4		
β_c	second channel flow exponent	3/2		
k_s	sheet conductivity	10^{-4}	10^{-2} – 10^{-5}	$\text{m}^{7/4} \text{kg}^{-1/2}$
k_c	channel conductivity	10^{-1}	5×10^{-1} – 10^{-3}	$\text{m}^{3/2} \text{kg}^{-1/2}$
E_{vr}	englacial void ratio	10^{-4}	10^{-3} – 10^{-5}	
l_c	sheet width below channel	2		m
A_m	moulin cross-sectional area	10		m^2
l_r	cavity spacing	2		m
h_r	basal bump height	0.085	0.05–0.1	m
b_{melt}	basal melt rate	5×10^{-3}	1 – 7×10^{-3}	m yr^{-1}
U_b	mean annual basal velocity [†]	150	100–200	m yr^{-1}
N_{moulin}	number of moulin [*]	2500	1000–4000	

[†] We tested both a transient and temporally constant basal velocity within these given ranges for mean annual basal velocity

^{*} We also ran an experiment in which melt was routed directly to the bed at each node (SHEET)

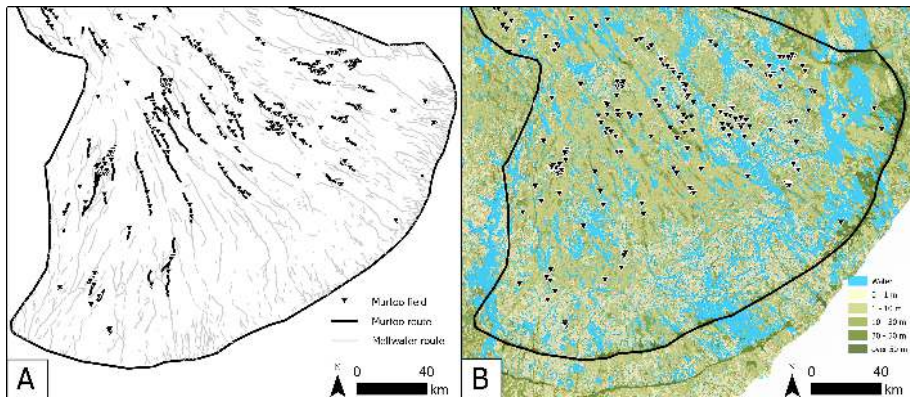


Figure A1. The distribution of meltwater routes, murtoos routes, and sediment in the Finnish Lake District Ice Lobe. **A)** Meltwater routes and murtoos routes as mapped by Ahokangas et al. (2021). There is a general absence of murtoos in the centre of the lobe 40–60 km from the ice margin. **B)** Sediment cover (GTK, Finland, 2010) showing thin sediment thickness in the terrain from which murtoos appear absent.

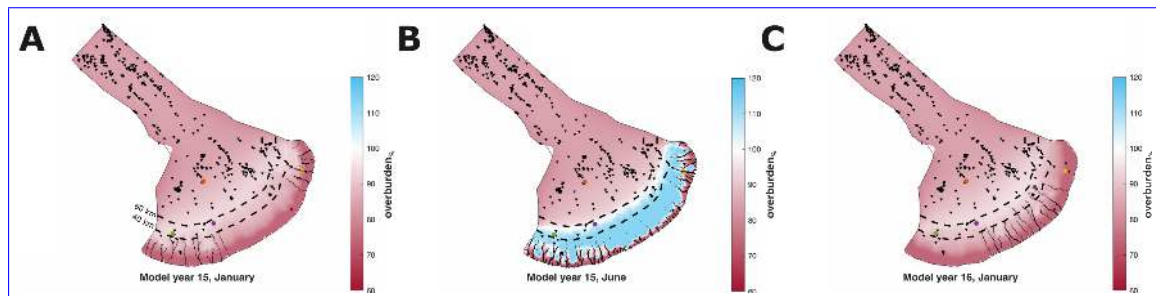


Figure A2. Overwinter channels and their influence on subsequent summer drainage. **A)** Modelled channels in January, model year 15 in the baseline run (black lines). Channels are present overwinter in the outer two thirds of the FLDIL. **B)** Modelled channels in June, model year 15, near to the start of the melt season. Note that channels in the outer two thirds are already well established compared to those in the central third of the FLDIL. **C)** Modelled channels in January, model year 2016. Note that winter channels are now visible in the central third of the FLDIL. In all panels, background panels shows water pressure as a percentage of ice overburden pressure. Murtoos are shown as inverted black triangles. Each channel is defined where the median channel discharge, Q_c , exceeds $1 \text{ m}^3 \text{ s}^{-1}$.

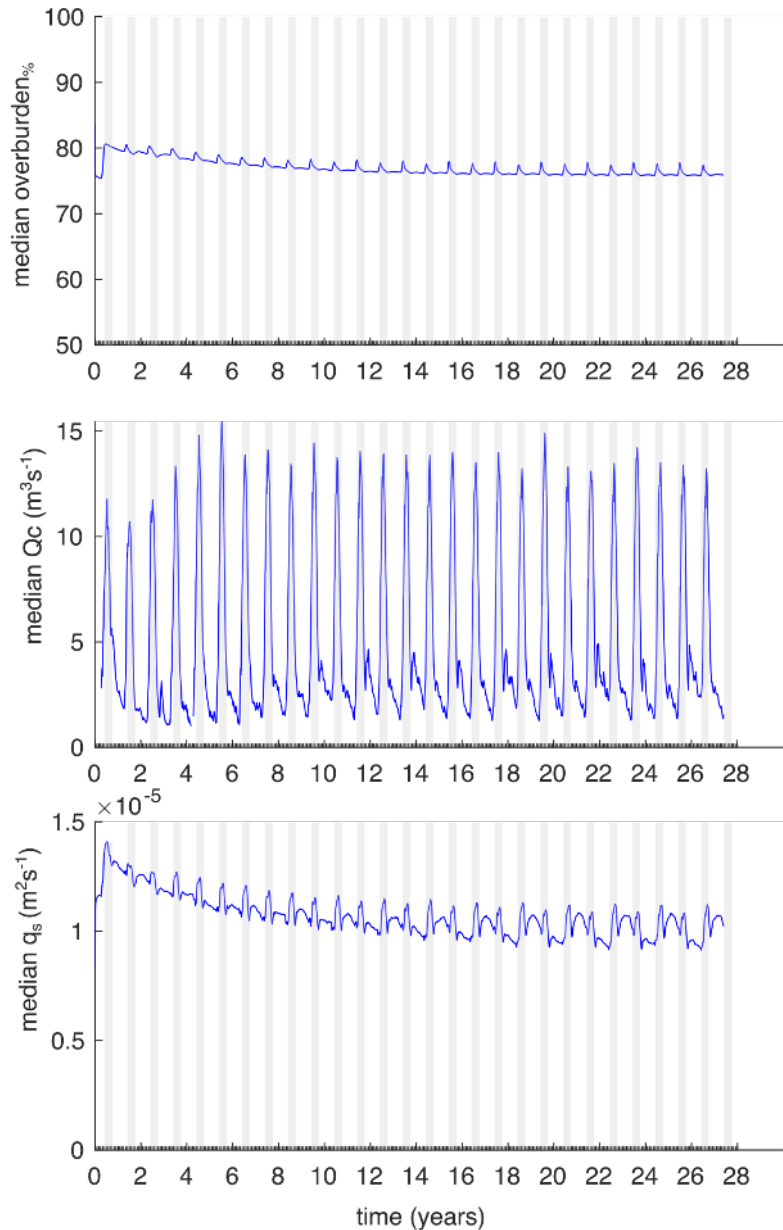


Figure A3. Median *overburden*%, channel discharge, Q_c , and sheet discharge, q_s over the full length of the baseline model run.

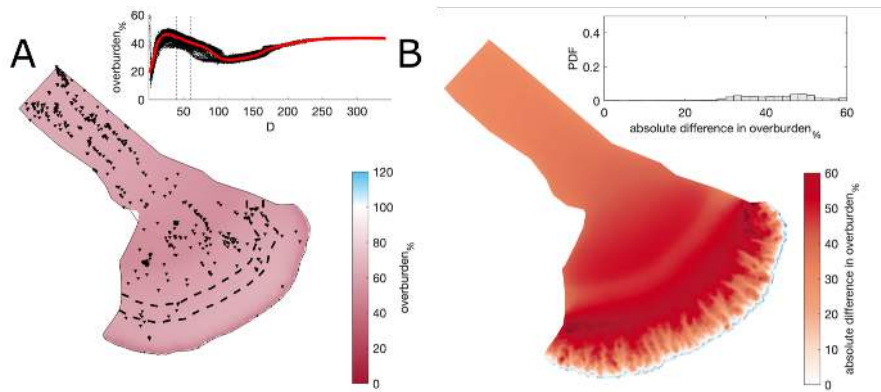


Figure A4. Comparison of the median summer system for sheet conductivity, $k_s = 10^{-2} \text{ m}^{7/4} \text{ kg}^{-1/2}$ against the baseline model run ($k_s = 10^{-4} \text{ m}^{7/4} \text{ kg}^{-1/2}$). **A**) Water pressure expressed as a percentage of overburden pressure, *overburden*%. Channels are shown as black lines where median discharge exceeds $1 \text{ m}^3 \text{ s}^{-1}$. **B**) Baseline median summer *overburden*% minus the $k_s = 10^{-2} \text{ m}^{7/4} \text{ kg}^{-1/2}$ median summer *overburden*%. The same figure caption applies for Figures A4–A32

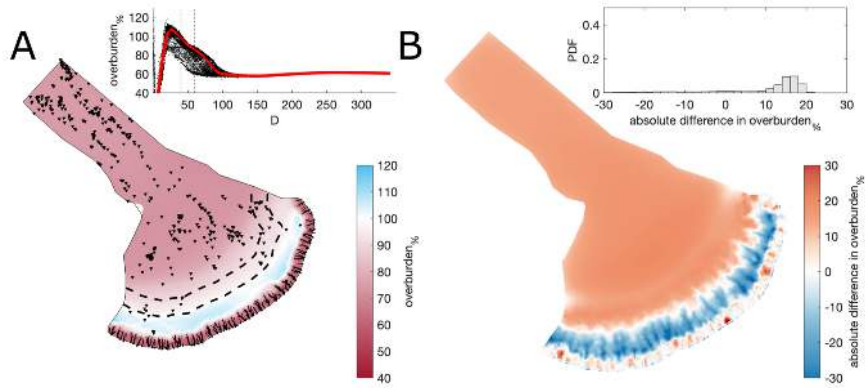


Figure A5. Comparison of the median summer system for sheet conductivity, $k_s = 10^{-3} \text{ m}^{7/4} \text{ kg}^{-1/2}$ against the baseline model run ($k_s = 10^{-4} \text{ m}^{7/4} \text{ kg}^{-1/2}$). The same figure caption as Figure A4 applies.

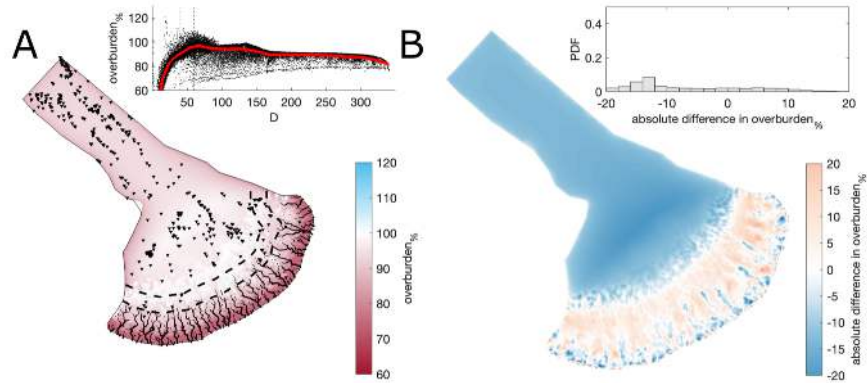


Figure A6. Comparison of the median summer system for sheet conductivity, $k_s = 10^{-5} \text{ m}^{7/4} \text{ kg}^{-1/2}$ against the baseline model run ($k_s = 10^{-4} \text{ m}^{7/4} \text{ kg}^{-1/2}$). The same figure caption as Figure A4 applies.

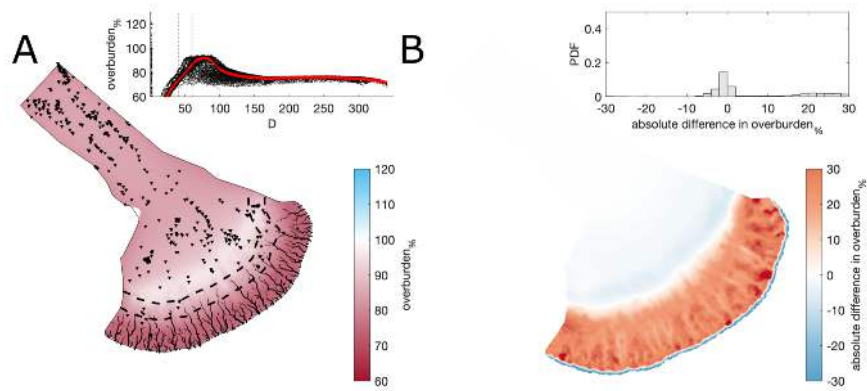


Figure A7. Comparison of the median summer system for channel conductivity, $k_c = 5 \times 10^{-1} \text{ m}^{3/2} \text{ kg}^{-1/2}$ against the baseline model run ($k_c = 10^{-1} \text{ m}^{3/2} \text{ kg}^{-1/2}$). The same figure caption as Figure A4 applies.

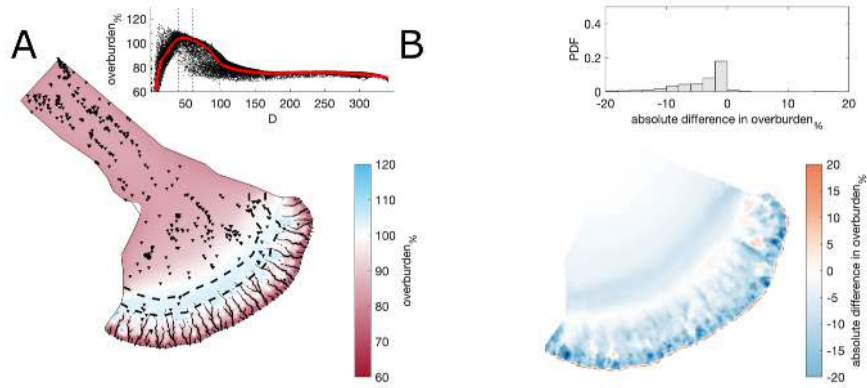


Figure A8. Comparison of the median summer system for channel conductivity, $k_c = 5 \times 10^{-2} \text{ m}^{3/2} \text{ kg}^{-1/2}$ against the baseline model run ($k_c = 10^{-1} \text{ m}^{3/2} \text{ kg}^{-1/2}$). The same figure caption as Figure A4 applies.

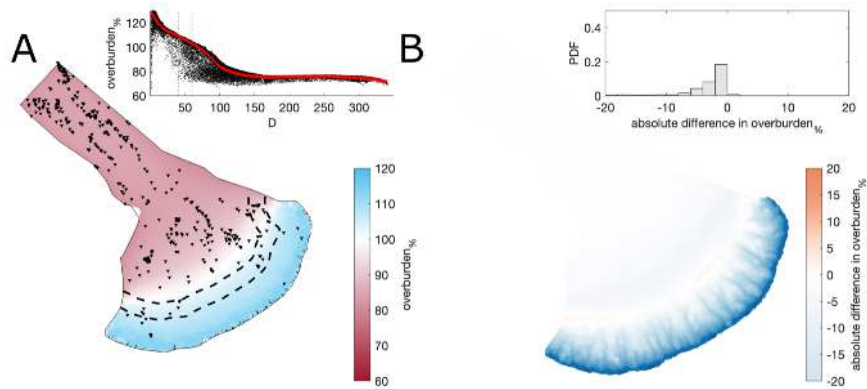


Figure A9. Comparison of the median summer system for channel conductivity, $k_c = 10^{-3} \text{ m}^{3/2} \text{ kg}^{-1/2}$ against the baseline model run ($k_c = 10^{-1} \text{ m}^{3/2} \text{ kg}^{-1/2}$). The same figure caption as Figure A4 applies.

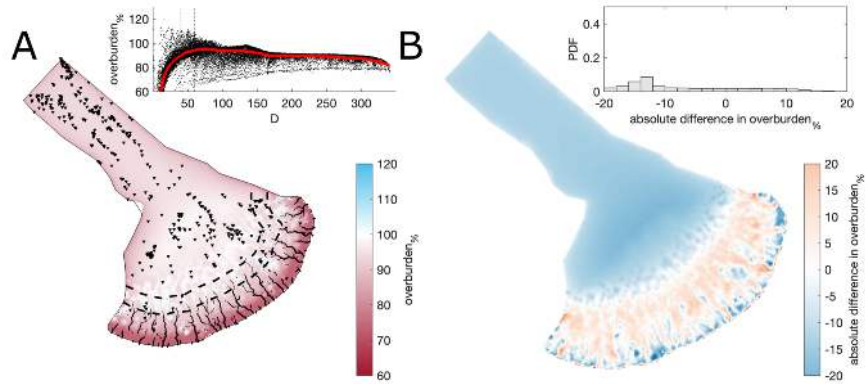


Figure A10. Comparison of the median summer system for moulin frequency, $N_{moulin} = 1000$ against the baseline model run ($N_{moulin} = 2500$). The same figure caption as Figure A4 applies.

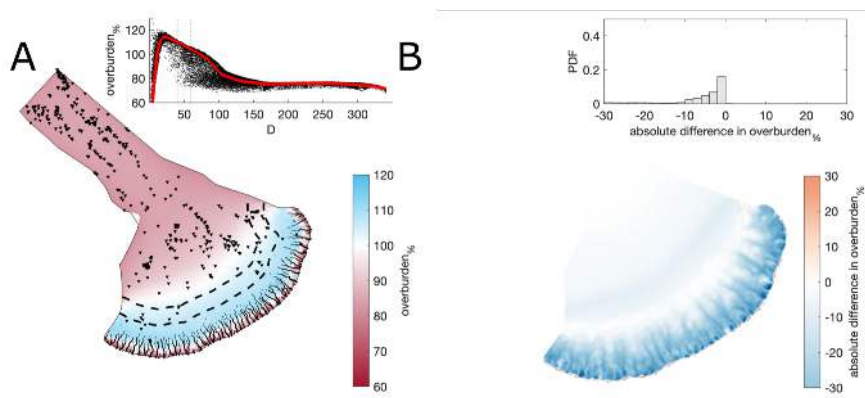


Figure A11. Comparison of the median summer system for moulin frequency, $N_{moulin} = 4000$ against the baseline model run ($N_{moulin} = 2500$). The same figure caption as Figure A4 applies.

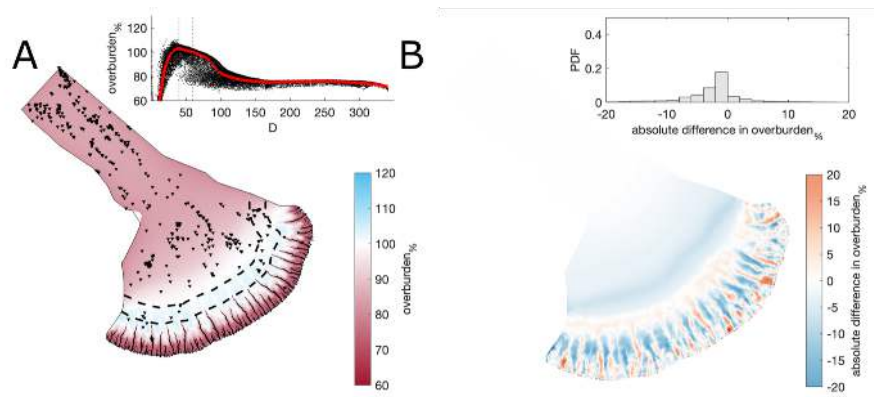


Figure A12. Comparison of the median summer system for where water was directly input at every nodes against the baseline model run ($N_{moulin} = 2500$). The same figure caption as Figure A4 applies.

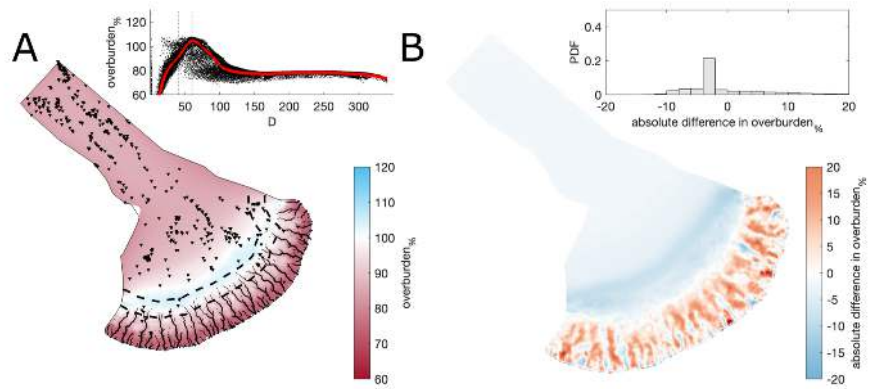


Figure A13. Comparison of the median summer system for a second random distribution of moulin frequency, $N_{moulin} = 2500$ against the baseline model run ($N_{moulin} = 2500$). The same figure caption as Figure A4 applies.

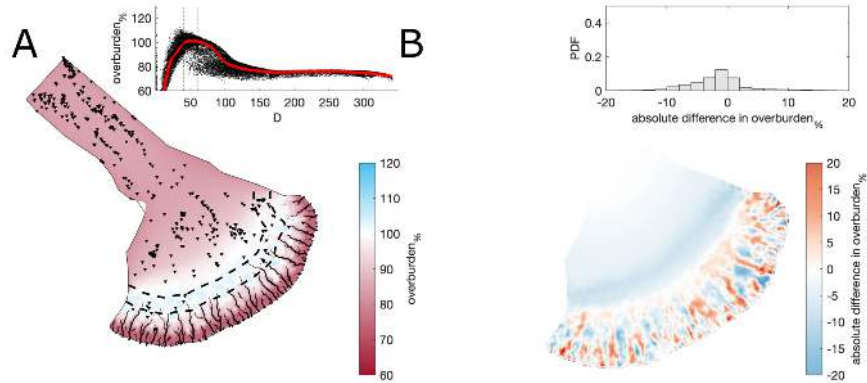


Figure A14. Comparison of the median summer system for a third random distribution of moulin frequency, $N_{moulin} = 2500$ against the baseline model run ($N_{moulin} = 2500$). The same figure caption as Figure A4 applies.

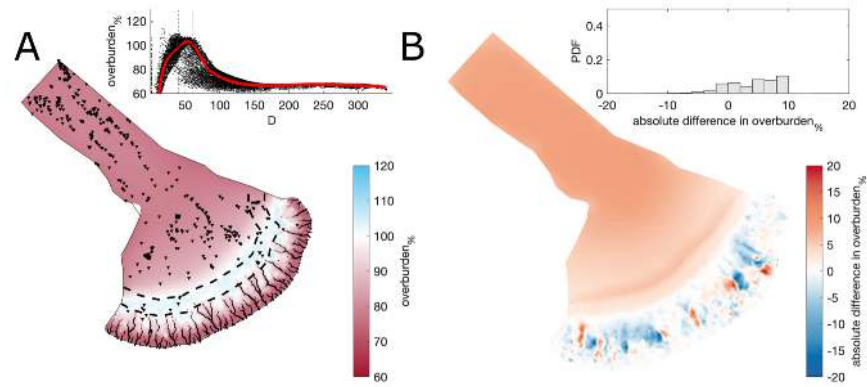


Figure A15. Comparison of the median summer system for basal melt rate, $b_{melt} = 1 \times 10^{-3} \text{ m yr}^{-1}$ against the baseline model run ($b_{melt} = 1 \times 10^{-3}$ $b_{melt} = 5 \times 10^{-3} \text{ m yr}^{-1}$). The same figure caption as Figure A4 applies.

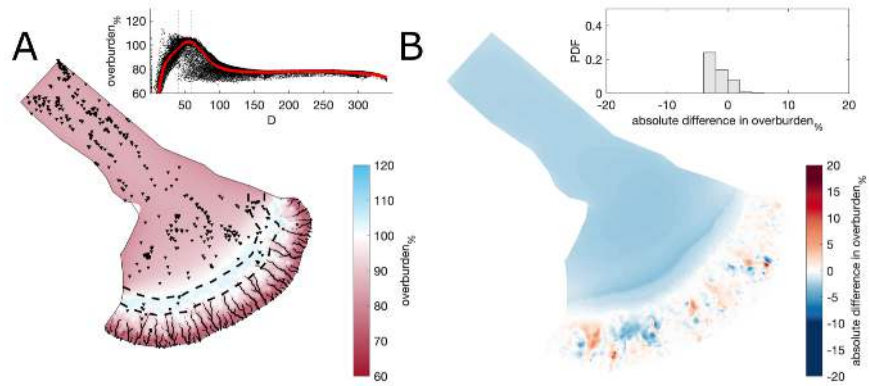


Figure A16. Comparison of the median summer system for basal melt rate, $b_{melt} = 1 \times 10^{-3} \text{ m yr}^{-1}$ against the baseline model run ($b_{melt} = 7 \times 10^{-3} \text{ m yr}^{-1}$). The same figure caption as Figure A4 applies.

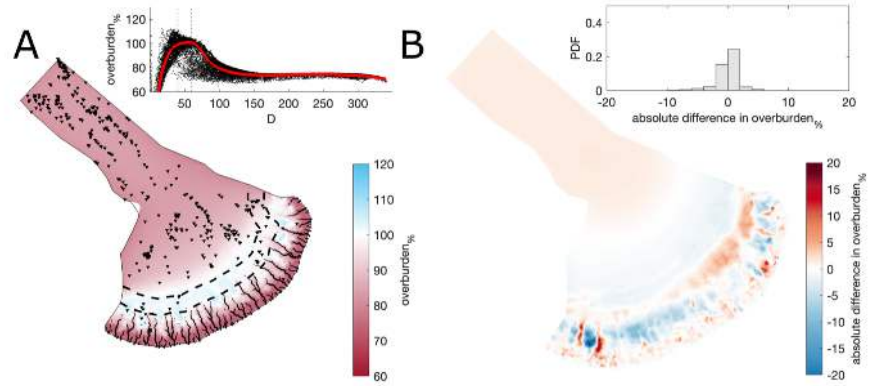


Figure A17. Comparison of the median summer system for basal bump height, $h_r = 0.1 \text{ m}$ against the baseline model run ($h_r = 0.085 \text{ m}$). The same figure caption as Figure A4 applies.

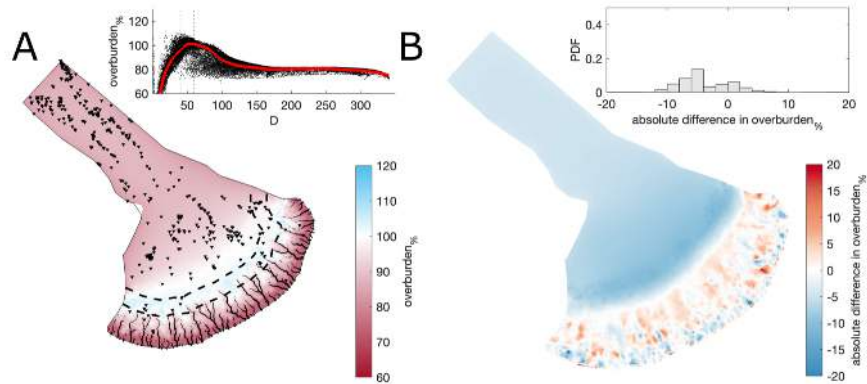


Figure A18. Comparison of the median summer system for basal bump height, $h_r = 0.05$ m against the baseline model run ($h_r = 0.085$ m). The same figure caption as Figure A4 applies.

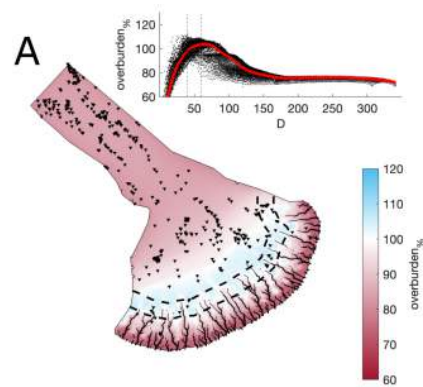


Figure A19. Comparison of a mesh that is not refined with respect to elevation against the baseline model run. The same figure caption as Figure A4 applies.

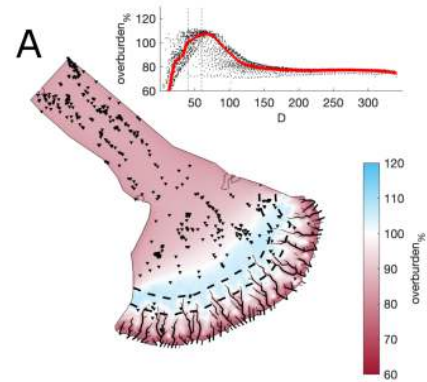


Figure A20. Comparison of a coarser mesh (edge length ~ 5 km) against the baseline model run. The same figure caption as Figure A4 applies.

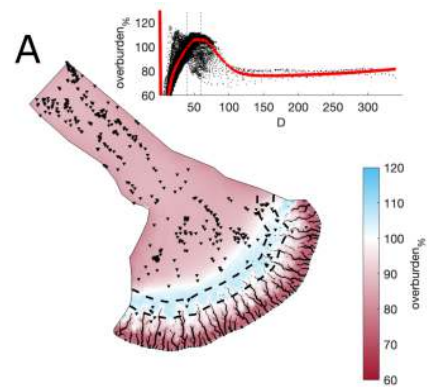


Figure A21. Comparison of a refined mesh (minimum edge length ≈ 300 m) < 80 km from the ice margin against the baseline model run. The same figure caption as Figure A4 applies.

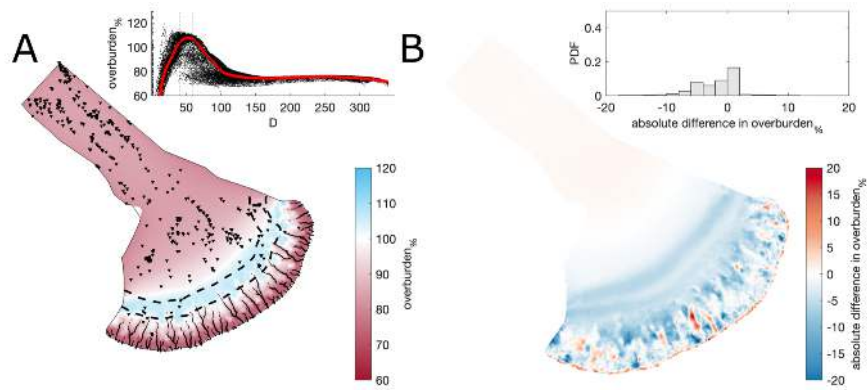


Figure A22. Comparison of a flat bed against the baseline model run. The same figure caption as Figure A4 applies.

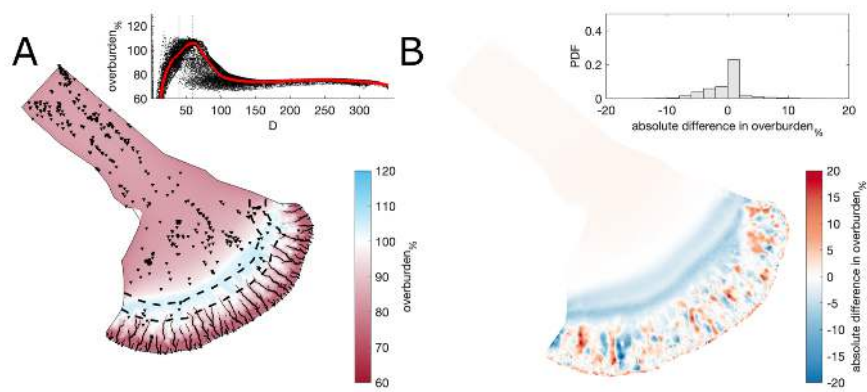


Figure A23. Comparison of a modern mesh (without subtracting Quaternary sediment thickness) against the baseline model run. The same figure caption as Figure A4 applies.

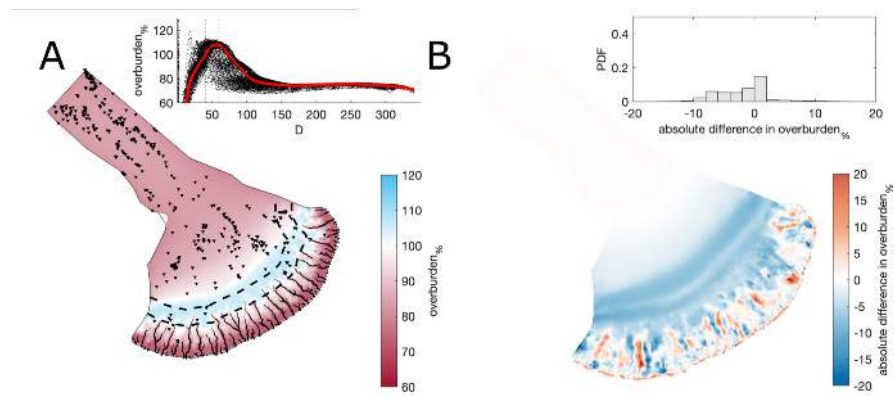


Figure A24. Comparison including lake bathymetry against the baseline model run. The same figure caption as Figure A4 applies.

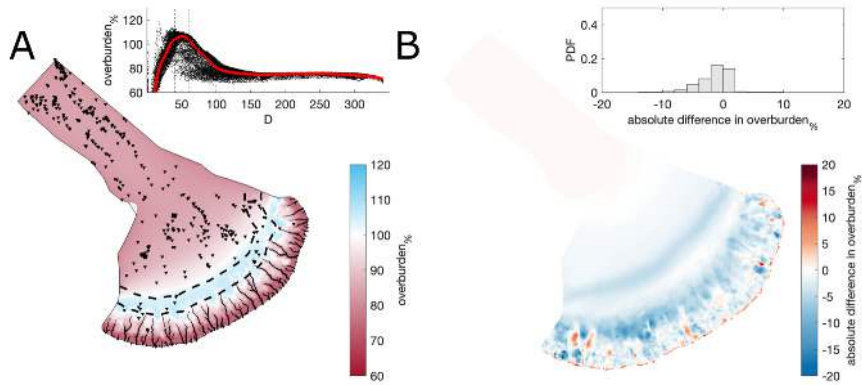


Figure A25. Comparison of a 30 m deep water body at the ice margin boundary against the baseline model run (land-terminating). The same figure caption as Figure A4 applies.

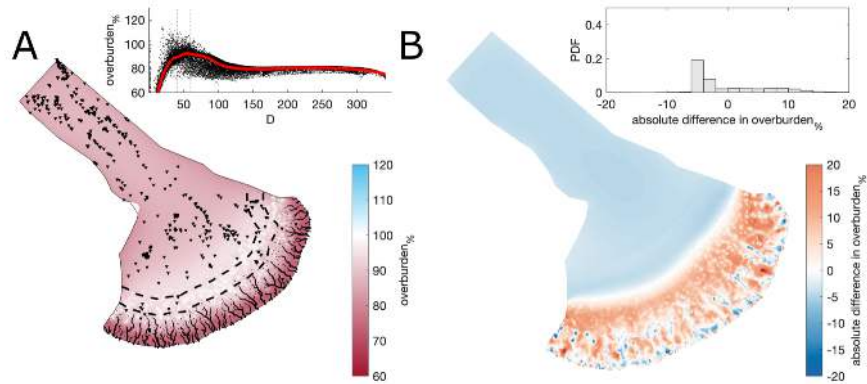


Figure A26. Comparison of the median summer system for an englacial void ratio, $E_{vr} = 10^{-3}$ against the baseline model run ($E_{vr} = 10^{-4}$). The same figure caption as Figure A4 applies.

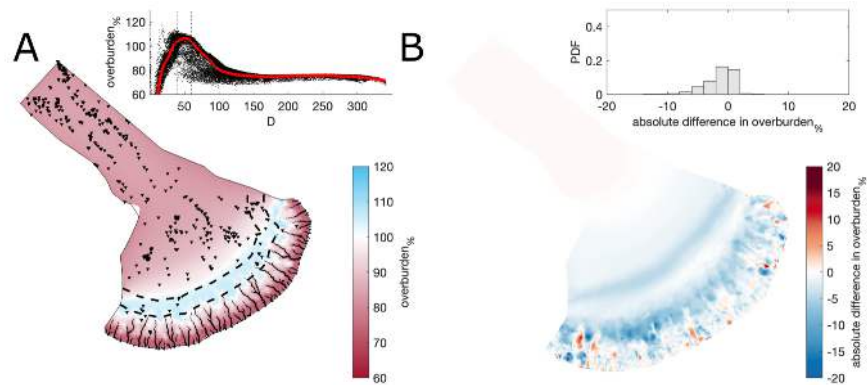


Figure A27. Comparison of the median summer system for an englacial void ratio, $E_{vr} = 10^{-5}$ against the baseline model run ($E_{vr} = 10^{-4}$). The same figure caption as Figure A4 applies.

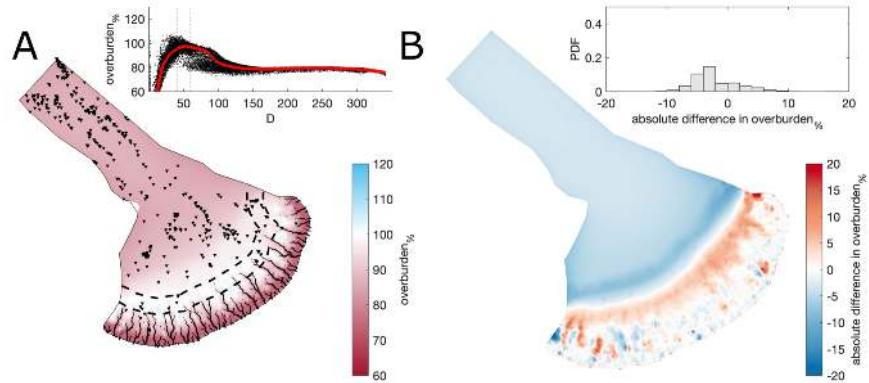


Figure A28. Comparison of the median summer system for a fixed basal velocity, $U_b = 100 \text{ m yr}^{-1}$ against the baseline model run ($U_b = 150 \text{ m yr}^{-1}$). The same figure caption as Figure A4 applies.

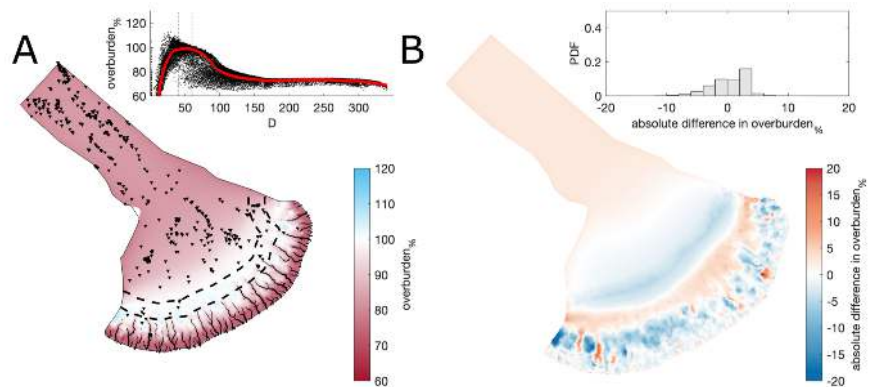


Figure A29. Comparison of the median summer system for a fixed basal velocity, $U_b = 200 \text{ m yr}^{-1}$ against the baseline model run ($U_b = 150 \text{ m yr}^{-1}$). The same figure caption as Figure A4 applies.

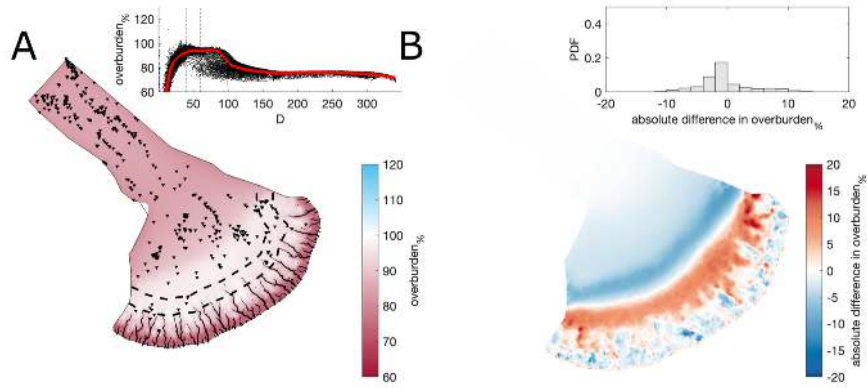


Figure A30. Comparison of the median summer system for a transient basal velocity, U_b with a median $U_b = 150 \text{ m yr}^{-1}$ against the fixed baseline model run ($U_b = 150 \text{ m yr}^{-1}$). The same figure caption as Figure A4 applies.

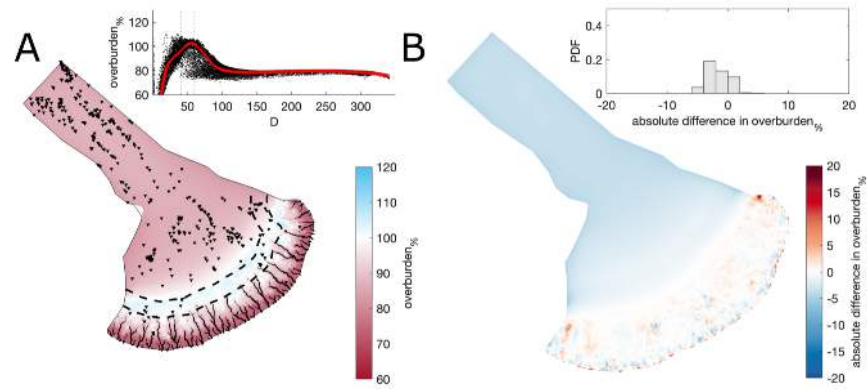


Figure A31. Comparison of the median summer system for a transient basal velocity, U_b with a median $U_b = 100 \text{ m yr}^{-1}$ against the fixed baseline model run ($U_b = 150 \text{ m yr}^{-1}$). The same figure caption as Figure A4 applies.

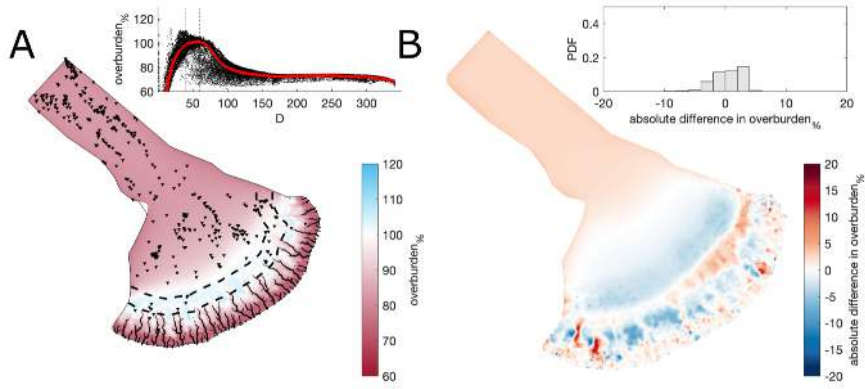


Figure A32. Comparison of the median summer system for a transient basal velocity, U_b with a median $U_b = 200 \text{ m yr}^{-1}$ against the fixed baseline model run ($U_b = 150 \text{ m yr}^{-1}$). The same figure caption as Figure A4 applies.

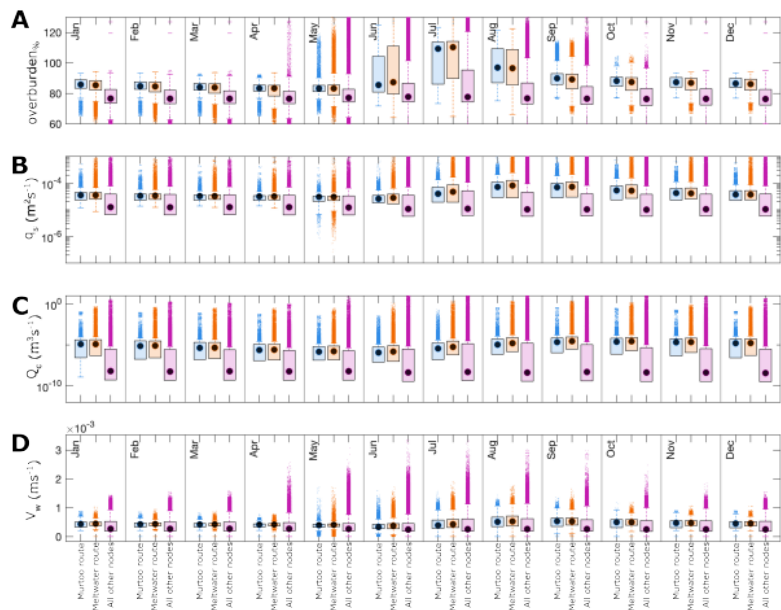


Figure A33. Boxplots of model parameters grouped by month for overburden (overburden%, **A**), sheet discharge (q_s , **B**), water velocity (V_w , **C**), and channel discharge (Q_c , **D**) during all model years at nodes between 40–60 km from the ice margin. As in Figure 5, nodes that fall within meltwater routes which do host murtoos (Murtoo free MRs) are shown in blue, nodes which fall within mapped meltwater routes that do not contain murtoos (Murtoo hosting MRs) are shown in orange, and all other nodes are shown in purple. Medians for each group are shown as black circles, and ‘outliers’—defined as points more than 150% of the interquartile range away from the upper and lower quartile—are shown as crosses.

Table A2. Tukey-Kramer HSD test of *overburden%* in meltwater routes, murtoo routes, and non-meltwater routes between 40–60 km from the ice margin. The upper and lower limits describe the 95% confidence intervals for the true mean difference, A-B is the difference between group means.

Month	Group A	Group B	Lower Limit	A-B	Upper limit	P-Value
January	meltwater route	murtoo route	-1.71	-1.30	-0.89	0.00
	all other nodes	murtoo route	-10.49	-10.12	-9.75	0.00
	meltwater route	all other nodes	8.58	8.82	9.06	0.00
February	meltwater route	murtoo route	-1.62	-1.21	-0.80	0.00
	all other nodes	murtoo route	-9.87	-9.50	-9.12	0.00
	meltwater route	all other nodes	8.05	8.29	8.52	0.00
March	meltwater route	murtoo route	-1.58	-1.17	-0.76	0.00
	all other nodes	murtoo route	-9.30	-8.93	-8.55	0.00
	meltwater route	all other nodes	7.52	7.75	7.99	0.00
April	meltwater route	murtoo route	-1.55	-1.14	-0.73	0.00
	all other nodes	murtoo route	-8.33	-7.96	-7.58	0.00
	meltwater route	all other nodes	6.58	6.82	7.06	0.00
May	meltwater route	murtoo route	-1.10	-0.69	-0.28	0.00
	all other nodes	murtoo route	-5.26	-4.89	-4.51	0.00
	meltwater route	all other nodes	3.96	4.20	4.43	0.00
June	meltwater route	murtoo route	0.70	1.12	1.54	0.00
	all other nodes	murtoo route	-8.56	-8.17	-7.79	0.00
	meltwater route	all other nodes	9.05	9.30	9.54	0.00
July	meltwater route	murtoo route	0.10	0.52	0.93	0.00
	all other nodes	murtoo route	-18.72	-18.34	-17.96	0.00
	meltwater route	all other nodes	18.61	18.85	19.10	0.00
August	meltwater route	murtoo route	-2.01	-1.59	-1.18	0.00
	all other nodes	murtoo route	-18.81	-18.43	-18.04	0.00
	meltwater route	all other nodes	16.59	16.83	17.08	0.00
September	meltwater route	murtoo route	-2.30	-1.88	-1.47	0.00
	all other nodes	murtoo route	-14.47	-14.09	-13.71	0.00
	meltwater route	all other nodes	11.97	12.21	12.45	0.00
October	meltwater route	murtoo route	-2.14	-1.72	-1.31	0.00
	all other nodes	murtoo route	-12.49	-12.11	-11.73	0.00
	meltwater route	all other nodes	10.15	10.39	10.63	0.00
November	meltwater route	murtoo route	-1.99	-1.57	-1.15	0.00
	all other nodes	murtoo route	-12.06	-11.68	-11.30	0.00
	meltwater route	all other nodes	9.87	10.11	10.36	0.00
December	meltwater route	murtoo route	-1.88	-1.46	-1.04	0.00
	all other nodes	murtoo route	-11.56	-11.17	-10.79	0.00
	meltwater route	all other nodes	9.47	9.72	9.96	0.00

Table A3. Tukey-Kramer HSD test of q_s in meltwater routes, murtoo routes, and non-meltwater routes between 40–60 km from the ice margin. The upper and lower limits describe the 95% confidence intervals for the true mean difference, A-B is the difference between group means.

Month	Group A	Group B	Lower Limit	A-B	Upper limit	P-Value
January	meltwater route	murtoo route	-5.07×10^{-7}	2.89×10^{-6}	6.28×10^{-6}	0.27
	all other nodes	murtoo route	-1.57×10^{-5}	-1.26×10^{-5}	-9.54×10^{-7}	0.00
	meltwater route	all other nodes	1.36×10^{-5}	1.55×10^{-5}	1.75×10^{-5}	0.00
February	meltwater route	murtoo route	-1.23×10^{-6}	2.19×10^{-6}	5.6×10^{-6}	0.88
	all other nodes	murtoo route	-1.39×10^{-5}	-1.08×10^{-5}	-7.69×10^{-6}	0.00
	meltwater route	all other nodes	1.1×10^{-5}	1.3×10^{-5}	1.5×10^{-5}	0.00
March	meltwater route	murtoo route	-2.05×10^{-6}	1.36×10^{-6}	4.77×10^{-6}	0.99
	all other nodes	murtoo route	-1.26×10^{-5}	-9.49×10^{-6}	-6.37×10^{-6}	0.00
	meltwater route	all other nodes	8.86×10^{-6}	1.08×10^{-5}	1.28×10^{-5}	0.00
April	meltwater route	murtoo route	-2.66×10^{-6}	7.6×10^{-7}	4.18×10^{-6}	0.99
	all other nodes	murtoo route	-1.14×10^{-5}	-8.28×10^{-6}	-5.15×10^{-6}	0.00
	meltwater route	all other nodes	7.05×10^{-6}	9.04×10^{-6}	1.10×10^{-5}	0.00
May	meltwater route	murtoo route	-2.92×10^{-6}	4.99×10^{-7}	3.92×10^{-6}	0.99
	all other nodes	murtoo route	-7.11×10^{-6}	-3.98×10^{-6}	-8.53×10^{-5}	0.00
	meltwater route	all other nodes	2.49×10^{-6}	4.48×10^{-6}	6.47×10^{-6}	0.00
June	meltwater route	murtoo route	9.57×10^{-7}	4.46×10^{-6}	7.97×10^{-6}	0.00
	all other nodes	murtoo route	6.04×10^{-6}	9.25×10^{-6}	1.25×10^{-5}	0.00
	meltwater route	all other nodes	-6.83×10^{-6}	-4.79×10^{-6}	-2.75×10^{-6}	0.00
July	meltwater route	murtoo route	1.36×10^{-5}	1.7×10^{-5}	2.05×10^{-5}	0.00
	all other nodes	murtoo route	9.95×10^{-6}	1.31×10^{-5}	1.63×10^{-5}	0.00
	meltwater route	all other nodes	1.89×10^{-6}	3.9×10^{-6}	5.91×10^{-6}	0.00
August	meltwater route	murtoo route	1.82×10^{-5}	2.17×10^{-5}	2.52×10^{-5}	0.00
	all other nodes	murtoo route	-9.99×10^{-6}	-6.79×10^{-6}	-3.59×10^{-6}	0.00
	meltwater route	all other nodes	2.65×10^{-5}	2.85×10^{-5}	3.05×10^{-5}	0.00
September	meltwater route	murtoo route	1.06×10^{-5}	1.41×10^{-5}	1.75×10^{-5}	0.00
	all other nodes	murtoo route	-2.33×10^{-5}	-2.02×10^{-5}	1.7×10^{-5}	0.00
	meltwater route	all other nodes	3.22×10^{-5}	3.42×10^{-5}	3.62×10^{-5}	0.00
October	meltwater route	murtoo route	5.67×10^{-6}	9.15×10^{-6}	1.26×10^{-5}	0.00
	all other nodes	murtoo route	-2.44×10^{-5}	-2.12×10^{-5}	-1.8×10^{-5}	0.00
	meltwater route	all other nodes	2.84×10^{-5}	3.04×10^{-5}	3.24×10^{-5}	0.00
November	meltwater route	murtoo route	2.52×10^{-6}	6×10^{-6}	9.48×10^{-6}	0.00
	all other nodes	murtoo route	-2.14×10^{-5}	-1.82×10^{-5}	-1.50×10^{-5}	0.00
	meltwater route	all other nodes	2.22×10^{-5}	2.42×10^{-5}	2.62×10^{-5}	0.00
December	meltwater route	murtoo route	7.23×10^{-7}	4.22×10^{-6}	7.71×10^{-6}	0.00
	all other nodes	murtoo route	-1.87×10^{-5}	-1.55×10^{-5}	1.23×10^{-5}	0.00
	meltwater route	all other nodes	1.77×10^{-5}	1.97×10^{-5}	2.18×10^{-5}	0.00

Table A4. Tukey-Kramer HSD test of Q_c in meltwater routes, murtoo routes, and non-meltwater routes between 40–60 km from the ice margin. The upper and lower limits describe the 95% confidence intervals for the true mean difference, A-B is the difference between group means.

Month	Group A	Group B	Lower Limit	A-B	Upper limit	P-Value
January	meltwater route	murtoo route	-7.57×10^{-3}	6.51×10^{-4}	8.87×10^{-3}	0.99
	all other nodes	murtoo route	-6.19×10^{-3}	1.34×10^{-3}	8.86×10^{-3}	0.99
	meltwater route	all other nodes	-5.47×10^{-3}	-6.86×10^{-4}	4.1×10^{-3}	0.99
February	meltwater route	murtoo route	-7.78×10^{-3}	5.08×10^{-4}	8.79×10^{-3}	0.99
	all other nodes	murtoo route	-6.72×10^{-3}	5.08×10^{-4}	8.44×10^{-3}	0.99
	meltwater route	all other nodes	-5.18×10^{-3}	-3.53×10^{-4}	4.47×10^{-3}	0.99
March	meltwater route	murtoo route	-7.86×10^{-3}	4.06×10^{-4}	8.677×10^{-3}	0.99
	all other nodes	murtoo route	-6.93×10^{-3}	6.3×10^{-4}	8.19×10^{-3}	0.99
	meltwater route	all other nodes	-5.04×10^{-3}	-2.24×10^{-4}	4.59×10^{-5}	0.99
April	meltwater route	murtoo route	-7.98×10^{-3}	3.07×10^{-4}	8.59×10^{-3}	0.99
	all other nodes	murtoo route	-7.10×10^{-3}	4.83×10^{-4}	8.06×10^{-3}	0.99
	meltwater route	all other nodes	-5×10^{-3}	-1.76×10^{-4}	4.65×10^{-3}	0.99
May	meltwater route	murtoo route	-8.02×10^{-3}	2.60×10^{-4}	8.54×10^{-3}	0.99
	all other nodes	murtoo route	-5.58×10^{-3}	2.01×10^{-3}	9.59×10^{-3}	0.99
	meltwater route	all other nodes	-6.57×10^{-3}	-1.75×10^{-3}	3.08×10^{-3}	0.99
June	meltwater route	murtoo route	-7.93×10^{-3}	5.65×10^{-4}	9.06×10^{-3}	0.99
	all other nodes	murtoo route	7.28×10^{-3}	1.51×10^{-2}	2.28×10^{-2}	0.00
	meltwater route	all other nodes	-1.94×10^{-2}	-1.45×10^{-2}	-9.54×10^{-3}	0.00
July	meltwater route	murtoo route	-6.22×10^{-3}	2.14×10^{-3}	1.05×10^{-2}	0.99
	all other nodes	murtoo route	3.20×10^{-2}	3.97×10^{-2}	4.73×10^{-2}	0.00
	meltwater route	all other nodes	-4.24×10^{-2}	-3.75×10^{-2}	-3.27×10^{-2}	0.00
August	meltwater route	murtoo route	-4.45×10^{-3}	4.02×10^{-3}	1.25×10^{-2}	0.99
	all other nodes	murtoo route	3.97×10^{-2}	4.74×10^{-2}	5.52×10^{-2}	0.00
	meltwater route	all other nodes	-4.84×10^{-2}	-4.34×10^{-2}	-3.85×10^{-2}	0.00
September	meltwater route	murtoo route	-4.64×10^{-3}	3.75×10^{-3}	1.21×10^{-2}	0.99
	all other nodes	murtoo route	2.24×10^{-2}	3.01×10^{-2}	3.78×10^{-2}	0.00
	meltwater route	all other nodes	-3.12×10^{-2}	-2.63×10^{-2}	-2.15×10^{-2}	0.00
October	meltwater route	murtoo route	-6.24×10^{-3}	2.19×10^{-3}	1.06×10^{-2}	0.99
	all other nodes	murtoo route	2.22×10^{-3}	9.94×10^{-3}	1.77×10^{-2}	0.00
	meltwater route	all other nodes	-1.27×10^{-2}	-7.75×10^{-3}	-2.84×10^{-3}	0.00
November	meltwater route	murtoo route	-7.16×10^{-3}	1.27×10^{-3}	9.70×10^{-3}	0.99
	all other nodes	murtoo route	-4.08×10^{-3}	3.63×10^{-3}	1.13×10^{-2}	0.99
	meltwater route	all other nodes	-7.27×10^{-3}	-2.36×10^{-3}	2.55×10^{-3}	0.99
December	meltwater route	murtoo route	-7.56×10^{-3}	9.10×10^{-4}	9.38×10^{-3}	0.99
	all other nodes	murtoo route	-5.57×10^{-3}	2.18×10^{-3}	9.94×10^{-3}	0.99
	meltwater route	all other nodes	-6.21×10^{-3}	-1.27×10^{-3}	3.66×10^{-3}	0.99

Table A5. Tukey-Kramer HSD test of V_W in meltwater routes, murtoo routes, and non-meltwater routes between 40–60 km from the ice margin. The upper and lower limits describe the 95% confidence intervals for the true mean difference, A-B is the difference between group means.

Month	Group A	Group B	Lower Limit	A-B	Upper limit	P-Value
January	meltwater route	murtoo route	1.41×10^{-6}	7.42×10^{-6}	1.34×10^{-5}	0.00
	all other nodes	murtoo route	-5.63×10^{-5}	-5.08×10^{-5}	-4.53×10^{-5}	0.00
	meltwater route	all other nodes	5.47×10^{-5}	5.82×10^{-5}	6.17×10^{-5}	0.00
February	meltwater route	murtoo route	1.11×10^{-6}	7.17×10^{-6}	1.32×10^{-5}	0.00
	all other nodes	murtoo route	-4.63×10^{-5}	-4.08×10^{-5}	-3.53×10^{-5}	0.00
	meltwater route	all other nodes	4.44×10^{-5}	4.80×10^{-5}	5.15×10^{-5}	0.00
March	meltwater route	murtoo route	7.90×10^{-7}	6.83×10^{-6}	1.29×10^{-5}	0.01
	all other nodes	murtoo route	-3.88×10^{-5}	-3.32×10^{-5}	-2.77×10^{-5}	0.00
	meltwater route	all other nodes	3.65×10^{-5}	4.01×10^{-5}	4.36×10^{-5}	0.00
April	meltwater route	murtoo route	1.06×10^{-6}	7.11×10^{-6}	1.32×10^{-5}	0.00
	all other nodes	murtoo route	-3.26×10^{-5}	-2.71×10^{-5}	-2.16×10^{-5}	0.00
	meltwater route	all other nodes	3.07×10^{-5}	3.42×10^{-5}	3.77×10^{-5}	0.00
May	meltwater route	murtoo route	1.73×10^{-6}	7.78×10^{-6}	1.38×10^{-5}	0.00
	all other nodes	murtoo route	-6.47×10^{-6}	-9.33×10^{-7}	4.61×10^{-6}	1.00
	meltwater route	all other nodes	5.19×10^{-6}	8.72×10^{-6}	1.22×10^{-5}	0.00
June	meltwater route	murtoo route	1.22×10^{-5}	1.84×10^{-5}	2.46×10^{-5}	0.00
	all other nodes	murtoo route	4.12×10^{-5}	4.69×10^{-5}	5.26×10^{-5}	0.00
	meltwater route	all other nodes	-3.21×10^{-5}	-2.85×10^{-5}	-2.48×10^{-5}	0.00
July	meltwater route	murtoo route	2.47×10^{-5}	3.09×10^{-5}	3.70×10^{-5}	0.00
	all other nodes	murtoo route	7.34×10^{-7}	6.33×10^{-6}	1.19×10^{-5}	0.01
	meltwater route	all other nodes	2.10×10^{-5}	2.45×10^{-5}	2.81×10^{-5}	0.00
August	meltwater route	murtoo route	1.46×10^{-5}	2.08×10^{-5}	2.70×10^{-5}	0.00
	all other nodes	murtoo route	-1.05×10^{-4}	-9.90×10^{-5}	-9.34×10^{-5}	0.00
	meltwater route	all other nodes	1.16×10^{-4}	1.20×10^{-4}	1.23×10^{-4}	0.00
September	meltwater route	murtoo route	2.52×10^{-6}	8.65×10^{-6}	1.48×10^{-5}	0.00
	all other nodes	murtoo route	-1.19×10^{-4}	-1.14×10^{-4}	-1.08×10^{-4}	0.00
	meltwater route	all other nodes	1.19×10^{-4}	1.22×10^{-4}	1.26×10^{-4}	0.00
October	meltwater route	murtoo route	8.15×10^{-6}	1.43×10^{-5}	2.05×10^{-5}	0.00
	all other nodes	murtoo route	-9.90×10^{-5}	-9.34×10^{-5}	-8.77×10^{-5}	0.00
	meltwater route	all other nodes	1.04×10^{-4}	1.08×10^{-4}	1.11×10^{-4}	0.00
November	meltwater route	murtoo route	6.68×10^{-6}	1.28×10^{-5}	1.90×10^{-5}	0.00
	all other nodes	murtoo route	-8.03×10^{-5}	-7.46×10^{-5}	-6.90×10^{-5}	0.00
	meltwater route	all other nodes	8.39×10^{-5}	8.75×10^{-5}	9.10×10^{-5}	0.00
December	meltwater route	murtoo route	3.95×10^{-6}	1.01×10^{-5}	1.63×10^{-5}	0.00
	all other nodes	murtoo route	-6.79×10^{-5}	-6.22×10^{-5}	-5.65×10^{-5}	0.00
	meltwater route	all other nodes	6.87×10^{-5}	7.23×10^{-5}	7.59×10^{-5}	0.00